

1 **Modulation of root growth by nutrient-defined fine-tuning of polar auxin**  
2 **transport**

3 Krisztina Ötvös<sup>1,4</sup>, Marco Marconi<sup>2</sup>, Andrea Vega<sup>3</sup>, Jose O' Brien<sup>3</sup>, Alexander Johnson<sup>1</sup>,  
4 Rashed Abualia<sup>1</sup>, Livio Antonielli<sup>4</sup>, Juan Carlos Montesinos<sup>1</sup>, Yuzhou Zhang<sup>1</sup>, Shutang Tan<sup>1</sup>,  
5 Candela Cuesta<sup>1</sup>, Christina Artner<sup>1</sup>, Eleonore Bouguyon<sup>5</sup>, Alain Gojon<sup>5</sup>, Jirí Friml<sup>1</sup>, Rodrigo  
6 A. Gutiérrez<sup>3</sup>, Krzysztof Wabnik<sup>2\*</sup> and Eva Benková<sup>1\*</sup>

7 Correspondence: Krzysztof Wabnik and Eva Benková

8 <sup>1</sup>*Institute of Science and Technology (IST) Austria, 3400 Klosterneuburg, Austria.*

9 <sup>2</sup>*Centro de Biotecnología y Genómica de Plantas (CBGP, UPM-INIA) Universidad Politécnica*  
10 *de Madrid (UPM) - Instituto Nacional de Investigación y Tecnología Agraria y Alimentaria*  
11 *(INIA), Campus de Montegancedo-UPM, 28223 Pozuelo de Alarcón, Madrid, Spain.*

12 <sup>3</sup>*Pontifical Catholic University of Chile, Santiago, Chile.*

13 <sup>4</sup>*Bioresources Unit, Center for Health & Bioresources, AIT Austrian Institute of Technology*  
14 *GmbH, 3430 Tulln, Austria.*

15 <sup>5</sup>*BPMP, Univ Montpellier, CNRS, INRAE, Institut Agro, Montpellier, France.*

16

17

18

19

20

21

22

23

24

25

26

## 27 **Abstract**

28 Nitrogen is an essential macronutrient and its availability in soil plays a critical role in plant  
29 growth, development and impacts agricultural productivity. Plants have evolved different  
30 strategies to sense and respond to heterogeneous nitrogen distribution. Modulating root system  
31 architecture, including primary root growth and branching, is among the most essential plant  
32 adaptations to ensure adequate nitrogen acquisition. However, the immediate molecular  
33 pathways coordinating the adjustment of root growth in response to varying nitrogen sources  
34 are poorly understood. Here, using a combination of physiological, live *in vivo* high- and super  
35 resolution imaging, we describe a novel adaptation strategy of root growth on available  
36 nitrogen source. We show that growth, *i.e.* tissue-specific cell division and elongation rates are  
37 fine-tuned by modulating auxin flux within and between tissues. Changes in auxin  
38 redistribution are achieved by nitrogen source dependent post-translational modification of  
39 PIN2, a major auxin efflux carrier, at an uncharacterized, evolutionary conserved phosphosite.  
40 Further, we generate a computer model based on our results which successfully recapitulate  
41 our experimental observations and creates new predictions that could broaden our  
42 understanding of root growth mechanisms in the dynamic environment.

43

## 44 **Introduction**

45 The ability to sense and adapt to fluctuations in nutrient availability is essential for the survival  
46 of all organisms. Every life form on our planet possesses delicate mechanisms for sensing and  
47 reacting to the variable nutrient status and adjusts their behavior to maintain growth or cope  
48 with stress caused by malnutrition. Mineral nutrients absorbed from the soil are major  
49 determinants of plant growth and development. Although required, fluctuations in their  
50 availabilities either to sub- or supra-optimal levels often have detrimental effects on plant  
51 metabolism and physiology, thereby attenuating plant fitness. Hence, the acquisition of mineral  
52 nutrients from the soil needs to be tightly controlled and endogenous levels within a plant body  
53 maintained at a physiological optimum level. At the molecular level, balancing nutrient  
54 acquisition with the plant's requirements implies that there is close communication between  
55 pathways controlling uptake, distribution and homeostasis of nutrients and the pathways  
56 coordinating plant growth and development.

57 The root system perceives and integrates local and systemic signals on the nutrient  
58 status to regulate activity of pathways mediating nutrient uptake and distribution. An important

59 component of the plant's nutrient management strategy involves a rapid modulation of the root  
60 growth and development. In response to nutrient availability, root meristem activity and  
61 elongation growth of primary root, as well as root branching, are adjusted in order to optimize  
62 nutrient provision to the plant body<sup>1</sup>. Production of new cells is essential for sustainable root  
63 growth; however, enhancement of the cell division machinery typically occurs within a range  
64 of hours<sup>2</sup>. In contrast, rapid modulation of cell elongation and manifold increase in cell volume  
65 would ensure faster growth responses<sup>3</sup>. Hence, in fluctuating environmental conditions root  
66 growth kinetics relies on the coordination of rapid elongation growth and adjustment of  
67 proliferation activity of the meristem.

68 Nitrogen (N) is a key macronutrient present in many key biological molecules and  
69 therefore constitutes a limiting factor in agricultural systems<sup>4</sup>. Although plants are dependent  
70 on an exogenous N supply and use nitrate (NO<sub>3</sub><sup>-</sup>), nitrite (NO<sub>2</sub><sup>-</sup>), and ammonium (NH<sub>4</sub><sup>+</sup>) as  
71 major sources of inorganic N, their preference for different inorganic forms depends on plant  
72 adaptation to soil<sup>4,5</sup>. For example; wheat, maize, canola, beans, sugar beet, *Arabidopsis* and  
73 tobacco grow preferentially on NO<sub>3</sub><sup>-</sup> nutrition, whereas, rice and pine grow on NH<sub>4</sub><sup>+</sup> nutrition.  
74 Fluctuations in both concentrations and the form of nitrogen sources available in the soil have  
75 prominent effects on root system growth and development<sup>6,7</sup>. Deficiency in nitrogen severely  
76 interferes with root elongation growth and development; low to medium availability of nitrogen  
77 enhances root growth and branching to promote the exploitation of this macronutrient, whereas  
78 high levels of availability might inhibit the elongation growth of primary and lateral roots<sup>8</sup>.  
79 When exposed to local nitrate-rich zones, the root system responds by enhancing lateral root  
80 (LR) outgrowth<sup>9-11</sup>. In the model plant *Arabidopsis thaliana*, the local availability of NO<sub>3</sub><sup>-</sup> and  
81 NH<sub>4</sub><sup>+</sup> seems to have complementary effects on the LR development (NH<sub>4</sub><sup>+</sup> stimulates  
82 branching, whereas NO<sub>3</sub><sup>-</sup> induces LR elongation<sup>11,12</sup>). These complex adaptive responses of  
83 the root organ to N sources and heterogeneity in availability are regulated by a combination of  
84 systemic and local signaling<sup>13</sup>. The impact of available sources of N on the root system is  
85 closely interconnected with the activity of plant hormones including auxin, cytokinin, ABA,  
86 ethylene and others<sup>14-16</sup>. In recent years, a number of studies have demonstrated that auxin  
87 biosynthesis, transport, and accumulation is altered in response to different N regimes in  
88 maize<sup>17,18</sup>, soybean<sup>19</sup>, pineapple<sup>20</sup> and *Arabidopsis thaliana*<sup>16,21-23</sup>. In *Arabidopsis*, several key  
89 auxin-related regulatory modules that respond to nitrogen availability were identified including  
90 *TAR2*, a gene involved in auxin biosynthesis, transporters of auxin such as *PIN-FORMED 1*  
91 (*PINI*), *PIN2*, *PIN4* and *PIN7* and molecular components, which control their subcellular  
92 trafficking<sup>21,24</sup>. At the level of auxin signaling, Auxin Response Factor *AUXIN RESPONSE*

93 *FACTOR 8* (*ARF8*, encoding a transcription factor of the auxin signaling machinery) was  
94 identified as a N responsive gene in the pericycle<sup>25</sup>. *ARF8* together with its associated  
95 microRNA167s is involved in the control of the ratio between LR initiation and emergence<sup>25–</sup>  
96 <sup>28</sup>. Another mechanism of nitrogen – auxin interplay underlying adaptation of the root system  
97 is mediated through NRT1.1, nitrate transceptor<sup>29</sup>. Its dual auxin-nitrate transport activity has  
98 been shown to play an important role in the adaptation of the root system, in particular, LR  
99 emergence to nitrate availability<sup>21,30</sup>.

100 Flexible modulation of primary root growth to fluctuations in nitrogen resources has  
101 been recognized as a prominent foraging strategy to optimize N exploitation<sup>31</sup>. However, the  
102 mechanisms that control the rapid reconfiguration of root growth dynamics in response to  
103 diverse N sources are still poorly understood. Here, to dissect the tissue and cellular  
104 mechanisms underlying the early phases of this adaptive process we focused on the primary  
105 responses of *Arabidopsis* roots to alterations in the available source of N such as NH<sub>4</sub><sup>+</sup> and  
106 NO<sub>3</sub><sup>-</sup>. We performed real time vertical confocal imaging to capture the earliest root responses  
107 after the replacement of NH<sub>4</sub><sup>+</sup> by NO<sub>3</sub><sup>-</sup>. We found that in roots supplied with NH<sub>4</sub><sup>+</sup>, local  
108 attenuation of meristematic activity in the epidermis results in the earlier transition of epidermal  
109 cells into elongation when compared to the cortex, thus generating asynchronous elongation of  
110 the adjacent tissues. Substitution of NH<sub>4</sub><sup>+</sup> for NO<sub>3</sub><sup>-</sup> led to a rapid enhancement of root growth  
111 associated with the simultaneous entrance of more cells at the root transition zone into  
112 elongation, and the subsequent re-establishment of a critical balance between cell proliferation  
113 and elongation. We demonstrate that root epidermis and cortex tissues supplemented with NO<sub>3</sub><sup>-</sup>  
114 synchronize their growth patterns. We show that the essential mechanism underlying this  
115 flexible adaptation of root growth involves nitrate-dependent fine-tuning of the auxin transport  
116 mediated by PIN2. In roots supplied with different forms of N, distinct localization patterns of  
117 PIN2 are generated as a result of dynamic PIN2 subcellular trafficking. Intriguingly,  
118 phosphoproteome analysis of PIN2 (Vega et al.) led to the identification of an uncharacterized  
119 nitrate-sensitive phosphorylation site. The functional characterization of PIN2 and its  
120 phosphor-variants suggest that the N source dependent modulation of PIN2 phosphorylation  
121 status has a direct impact on the flexible adjustment of PIN2 localization pattern, and thereby  
122 facilitates the adaptation of root growth to varying forms of N supply. Finally, we integrated  
123 experimental data regarding the nitrogen-dependent root growth into a quantitative computer  
124 model. Our computer model recapitulated *in planta* patterning from a minimal set of  
125 assumptions and made predictions that were tested experimentally. Taken together, we present  
126 a quantitative mechanistic model of how *Arabidopsis* primary root growth is fine-tuned to

127 different N sources. We hypothesize, that the flexible modulation of growth patterns relying  
128 on nutrient response on auxin transport is an important part of the intelligent strategy, to enable  
129 plant root adaption to the dynamically changing environment and thus maintain its sustainable  
130 growth.

131

## 132 **Results**

### 133 ***Root growth rapidly adjusts to form of nitrogen source***

134 To explore how primary root responds and adapts to different forms of N, *Arabidopsis*  
135 seedlings were grown on  $\text{NH}_4^+$  as an exclusive N source for five days (5 DAG) and afterward  
136 transferred on media containing either  $\text{NH}_4^+$  or  $\text{NO}_3^-$ . We found that replacement of  $\text{NH}_4^+$  by  
137  $\text{NO}_3^-$  rapidly enhanced root length and already 6 hours after transfer (HAT), roots were  
138 significantly longer compared to these supplied with  $\text{NH}_4^+$  (Fig. S1a). In general, root growth  
139 is determined by the elongation of cells, which are constantly produced by the root apical  
140 meristem. To study processes that underlie the adaptation of root growth to different forms of  
141 N a vertical confocal microscope equipped with a root tracker system was employed. Using  
142 this setup, we were able to detect and monitor the earliest root responses with a high cellular  
143 resolution<sup>32</sup>. To minimize the interference of physiological conditions for seedling  
144 development, a light-dark regime was maintained in course of the root tracking. After the  
145 transfer of wild type (Col-0) seedlings to  $\text{NH}_4^+$  containing medium root growth rate (RGR) was  
146 enhanced, presumably as a response to stress caused by transfer of seedlings to a fresh plate.  
147 Within ~120 min RGR stabilized at an average speed of  $1.37 \pm 0.025 \mu\text{mmin}^{-1}$ . Transition to  
148 dark period correlated with a rapid drop of RGR to  $0.98 \pm 0.029 \mu\text{mmin}^{-1}$ , which was  
149 maintained during the dark phase and at the light recovered again to  $1.27 \pm 0.048 \mu\text{mmin}^{-1}$ .  
150 Seedlings transferred to  $\text{NO}_3^-$  reacted by an increase of RGR to  $1.77 \pm 0.042 \mu\text{mmin}^{-1}$  and  
151 similarly to roots on  $\text{NH}_4^+$ , during the dark period their RGR decelerated and was retrieved to  
152  $1.81 \pm 0.051 \mu\text{mmin}^{-1}$  at the light (Fig. 1a, Supplemental video 1). Hence, provision of  $\text{NO}_3^-$   
153 caused a rapid enhancement of RGR when compared to  $\text{NH}_4^+$ , but it did not interfere with its  
154 circadian rhythmicity<sup>33</sup>.

155 To gain more insight into the mechanistic basis underlying the rapid increase of root  
156 length after substitution of  $\text{NH}_4^+$  for  $\text{NO}_3^-$ , we focused on cells in the transition zone (TZ). The  
157 TZ is located between the root apical meristem and elongation zone, and cells while passing  
158 this developmental zone undergo essential modifications associated with their transition from  
159 the proliferative to the elongation phase<sup>34,35</sup> (Fig. 1b). Time-lapse experiments capturing root

160 growth from 2 to 3.76 hours after transfer combined with a tracking of cell membranes pointed  
161 at differences in the elongation pattern of epidermal cells in roots supplied with either  $\text{NH}_4^+$  or  
162  $\text{NO}_3^-$ . While, in roots supplemented with  $\text{NH}_4^+$  only a few epidermal cells enter into elongation  
163 phase. Provision of  $\text{NO}_3^-$  increased number of elongating cells in the TZ (Fig. 1b, Supplemental  
164 video 2). Next, we analyzed in detail 18 roots 12 HAT on either  $\text{NH}_4^+$  or  $\text{NO}_3^-$  and measured  
165 length of the epidermal cells across the meristematic, transition and the start of the elongation  
166 zones. The analyses suggested that on  $\text{NO}_3^-$  more epidermal cells enter into transition phase, as  
167 indicated by an increased number of cells 30-40  $\mu\text{m}$  long when compared to roots on  $\text{NH}_4^+$   
168 (Fig. S1b). Despite the stimulating impact of  $\text{NO}_3^-$  on cell transition into the elongation phase,  
169 no differences in the maximal length of fully differentiated epidermal cells between roots on  
170  $\text{NO}_3^-$  and  $\text{NH}_4^+$  were detected (Fig. S1c). This suggests that  $\text{NO}_3^-$  promoted root growth is a  
171 result of modulated elongation kinetics of cells along the longitudinal root growth axis and not  
172 increase of the maximal cell length.

173 To sustain root growth, the rate of cell elongation and differentiation has to be tightly  
174 balanced with the production of new cells in the root meristem<sup>36</sup>. Hence, enhanced growth of  
175 cells after replacement of  $\text{NH}_4^+$  by  $\text{NO}_3^-$  could lead to depletion of the meristem if expansion  
176 of cells would prevail over a new cell production. To examine how root meristem adapt to  
177 change in N supply, cell length and frequency of divisions in epidermis and cortex along the  
178 longitudinal root growth axis were closely inspected 12 HAT. Surprisingly, length of epidermal  
179 cells started to increase from the 11<sup>th</sup> cell on (cell number was counted from quiescent center  
180 (QC)) in roots supplied with  $\text{NH}_4^+$  (Fig. 1c and Supplemental Document 1a-b). In contrast,  
181 roots on  $\text{NO}_3^-$  exhibited an increase in size from the 13<sup>th</sup> epidermal cells (Fig. 1d, S1d  
182 Supplemental Document 1a-b). Unlike the epidermis, the length profiles of cortex cells were  
183 not significantly different between roots supplied with either  $\text{NH}_4^+$  or  $\text{NO}_3^-$  (Fig. S1e,  
184 Supplemental Document 1a-b). Therefore, the growth of epidermal and cortex cells in roots on  
185  $\text{NH}_4^+$  displayed clearly asynchronous behavior (Fig. 1c, d). Additionally, a machine learning  
186 approach was applied to regression analysis for assessing the importance of each variable (i.e.  
187 treatments: ammonium and nitrate, tissues: epidermis and cortex, cell positions) on cell length  
188 differences. Analysis of deviance was followed by estimated marginal mean (emmean)  
189 comparisons of cell lengths in different tissues (epidermis vs cortex) at each cell position (1-  
190 20 from QC) for each treatment (ammonium vs nitrate). The results show that ammonium and  
191 nitrate treatments affect the cell positions differentially: epidermal cells from the 17<sup>th</sup> up to the  
192 20<sup>th</sup> position are significantly longer on ammonium while cell length in cortex is not affected



193 by the treatments. (Supplemental Document 1a-b). Results were confirmed by recursive  
194 partitioning analysis and shown in a decision tree (Supplemental Document 1c).

195 The distinct elongation pattern of epidermal and cortex cells detected in roots on  $\text{NH}_4^+$   
196 can only be sustained if cell divisions in cortex compensate for an earlier start of cell elongation  
197 in the epidermis. Accordingly, the scoring of cell division events (visualized by DAPI) revealed  
198 a higher number of mitotic events in cortex compared to epidermal cells in roots transferred to  
199  $\text{NH}_4^+$ . On  $\text{NO}_3^-$  similar frequency of cell divisions in both epidermal and cortex cell files was  
200 observed (Fig. 1e, Fig. S2a). Finally, monitoring of the cell cycle reporter *CyclinB::GUS*  
201 expression 2 days after transfer (DAT) to either  $\text{NH}_4^+$  or  $\text{NO}_3^-$  revealed enhanced reporter  
202 expression and overall enlargement of the meristematic zone in roots supplemented with  $\text{NO}_3^-$   
203 (Fig. S2b).

204 Altogether, these data indicate that roots adopt distinct growth strategies involving fine-  
205 tuning of cell division and expansion across adjacent tissues to adapt to different forms of N.  
206 In roots supplied with  $\text{NH}_4^+$ , the meristematic activity of epidermal cells is attenuated, which  
207 results in their earlier transition into the elongation phase when compared to the cortex.  
208 Provision of  $\text{NO}_3^-$  increases the number of epidermal cells in the TZ (Fig. 1b, S1b), which is  
209 one of the earliest detectable adaptive responses. Subsequently, within twelve hours, the  
210 frequency of cell division in the epidermis increases, which results in shift of balance between  
211 cell division and elongation and more synchronized growth of cortex and epidermis.  
212 Eventually, a long-term supply of  $\text{NO}_3^-$  enables enlargement of the root apical meristem  
213 compared to roots supplied with  $\text{NH}_4^+$ .

#### 214 ***Level and pattern of auxin activity in roots are modulated by form of nitrogen source***

215 The plant hormone auxin is an essential endogenous regulatory cue that determines key  
216 aspects of root growth. Interference with auxin biosynthesis<sup>37</sup>, signaling<sup>38</sup> or distribution<sup>39</sup> at  
217 the root tip has a significant impact on the meristem maintenance, and transition of  
218 meristematic cells into elongation and differentiation phase. Distinct growth patterns observed  
219 in roots supplemented with different forms of N prompted us to monitor distribution of auxin  
220 at the root tip. Quantification of the LUCIFERASE activity in protein extracts from roots  
221 carrying the auxin sensitive *DR5::LUCIFERASE* reporter revealed that already one hour after  
222 transfer to  $\text{NO}_3^-$  containing medium auxin response increases when compared to roots  
223 transferred to  $\text{NH}_4^+$  supplemented medium (Fig. S3a). To closely inspect the auxin distribution  
224 in a cell lineage-specific manner a ratiometric degradation based *R2D2* auxin reporter was  
225 implemented<sup>40</sup>. In accordance with observations based on the *DR5::LUCIFERASE* reporter, a

226 decreased ratio between DII-Venus (green) and mDII-Tomato (red) fluorescent signals  
227 indicated increased levels of auxin activity in the central cylinder of roots in response to  
228 replacement of  $\text{NH}_4^+$  by  $\text{NO}_3^-$  (Fig. S3b).

229 In addition, we focused on the detailed profiling of the R2D2 reporter in the epidermis  
230 and the cortex (Fig. S3c). Interestingly, we detected an overall increase of auxin activity in  
231 epidermal cells when compared to cortex cells in roots supplied with  $\text{NH}_4^+$ , whereas no  
232 difference between these two cell files were detected in roots on  $\text{NO}_3^-$  (Fig. 2a, b). Furthermore,  
233 on  $\text{NH}_4^+$  there was an increase of auxin activity in epidermal cells when compared to cortex  
234 cells (starting from ~ 11<sup>th</sup> cell from the QC), while in roots supplied with  $\text{NO}_3^-$  the auxin activity  
235 profiles followed similar trends of steady increase in both cortex and epidermal cell files (Fig.  
236 2a, b). Altogether, these analyses indicate that pattern of auxin activity at root meristems might  
237 adapt to specific N conditions. In roots supplied with  $\text{NH}_4^+$ , the early steep gradient of auxin  
238 signaling in epidermal cells correlates with their early transition into the rapid elongation phase.  
239 Whereas in cortex cells, auxin reaches concentrations which might drive elongation in more  
240 proximal cells. Substitution of  $\text{NH}_4^+$  by  $\text{NO}_3^-$  attenuates differences in profiles of the auxin  
241 distribution between the cortex and the epidermal cell files, which would lead to the  
242 synchronized cell growth (Fig. 2a, b compared to Fig. 1c, d).

#### 243 *Nitrogen source affects basipetal auxin transport*

244 Directional cell-to-cell transport of auxin significantly contributes to the establishment of the  
245 auxin activity pattern at the root tip. The Polar auxin transport (PAT) machinery, composed of  
246 AUX/LAX influx and PIN efflux carriers, directs the flow of auxin from the shoot acropetally  
247 through the stele towards the root tip; from where it is via epidermis basipetally redistributed  
248 to the elongation zone. At the TZ, auxin might be redirected from the basipetal stream across  
249 the cortex, endodermis and pericycle back to stele and root tip, thereby fine-tuning levels of  
250 auxin at the TZ<sup>41,42</sup>. The modulation of auxin activity pattern in the outer tissues detected after  
251 the replacement of  $\text{NH}_4^+$  for  $\text{NO}_3^-$  suggests that there are alterations of the basipetal auxin  
252 transport. To explore how different forms of N affect the flow of auxin in basipetal direction,  
253 transport assays using radioactively labeled auxin (<sup>3</sup>H-IAA) were performed. Six hours after  
254 applying <sup>3</sup>H-IAA to the root tip, radioactivity in the proximal zone of the primary roots supplied  
255 with  $\text{NH}_4^+$  was significantly lower when compared to roots on either  $\text{NO}_3^-$  supplemented or  
256 standard Murashige and Skoog (MS) medium (Fig. 3A). These results indicate that basipetal  
257 auxin transport can be modulated by available source of N, and provision of  $\text{NO}_3^-$  enhances  
258 flux of auxin in shootward direction when compared to  $\text{NH}_4^+$ .



259 The PIN2 auxin efflux carrier is amongst the principal components of PAT mediating  
260 basipetal transport of auxin in roots<sup>43,44</sup>. To test whether adjustment of the basipetal auxin flow  
261 in response to different sources of nitrogen is dependent on activity of PIN2, we tested *eir1-4*,  
262 a mutant defective in this efflux transporter. In agreement with previous reports<sup>45</sup>, a  
263 significantly lower radioactivity in the proximal root zone of the *eir1-4* was detected when  
264 compared to wild type roots on MS medium (Fig. 3a). Noteworthy, no radioactivity increase  
265 in the proximal zone of *eir1-4* roots was observed in roots supplied with NO<sub>3</sub><sup>-</sup> when compared  
266 to NH<sub>4</sub><sup>+</sup> (Fig. 3a), pointing towards PIN2 function in the flexible adjustment of the basipetal  
267 auxin flow in response to form of N source. To further examine the role of the PIN2 mediated  
268 transport in establishment of distinct auxin patterns at root tips supplemented with different  
269 forms of N, we monitored the auxin sensitive reporter DII-Venus and its stabilized auxin  
270 responsive analog mDII-Venus<sup>46</sup> as a reference in *eir1-4* and Col-0 roots. The expression  
271 pattern of DII-Venus reporter in Col-0 roots was largely consistent with what we observed  
272 using the R2D2 reporter (Fig. S4a-b). In Col-0 roots supplied with NH<sub>4</sub><sup>+</sup>, a reduced DII-Venus  
273 signal indicated a higher auxin activity in epidermal cells when compared to the cortex. Also,  
274 consistently with the R2D2 reporter, a steeper slope of auxin activity in epidermis when  
275 compared to cortex (with onset at ~8<sup>th</sup> cell distance from QC) was detected in roots supplied  
276 with NH<sub>4</sub><sup>+</sup>, whereas in roots on NO<sub>3</sub><sup>-</sup>, auxin activity both in epidermis and cortex followed  
277 similar trends (Fig. 3b, c compared to Fig. 2a, b and Fig. S4a, b). *eir1-4* was severely affected  
278 in adjustment of auxin pattern to different N sources. When compared to Col-0, overall higher  
279 levels of auxin activity in both epidermal and cortex cells and a shallower slope of auxin  
280 activity increase in the epidermis was observed in *eir1-4* roots supplied with NH<sub>4</sub><sup>+</sup>. As a result,  
281 the difference in auxin activity profiles between the cortex and the epidermis in *eir1-4* was less  
282 pronounced than in wild type roots (Fig. 3d compared to Fig. 3b and Fig. S4a). On NO<sub>3</sub><sup>-</sup>, overall  
283 profiles of auxin activity in epidermis and cortex of *eir1-4* followed similar trends,  
284 characterized by shallow slope along the longitudinal root growth axis (Fig. 3e, Fig. S4b).  
285 Importantly, expression pattern of the auxin insensitive mDII-Venus reference construct  
286 remained largely unchanged under all tested conditions in both wild type and *eir1-4* (Fig. S4c,  
287 d). Altogether, our results point at an important role of PIN2 dependent basipetal auxin  
288 transport in adjustment of auxin activity pattern in roots to specific N conditions.

### 289 ***PIN2 mediates root growth adaptation to nitrogen resources***

290 To further examine the role of PIN2 mediated basipetal auxin transport in root growth  
291 adaptation to different sources of N, *eir1-4* and *eir1-1* mutant alleles of *PIN2* were analyzed.

292 Unlike in wild type, no significant increase in root length was detected 1 DAT in either *eir1-4*  
293 or *eir1-1* seedlings on  $\text{NO}_3^-$  when compared to  $\text{NH}_4^+$  supplemented medium (Fig. S5a). Closer  
294 inspection of the RGR in real time using vertical confocal - root tracking set up showed that  
295 after transfer on  $\text{NH}_4^+$  growth of the *eir1-4* roots stabilized at  $1.47 \pm 0.041 \mu\text{mmin}^{-1}$  and  $1.35$   
296  $\pm \mu\text{mmin}^{-1}$  during light and dark period, respectively. However, no significant increase of RGR  
297 after transfer to  $\text{NO}_3^-$  containing medium could be observed (Fig. 4a). These results strongly  
298 support an essential role of PIN2 mediated basipetal auxin transport in rapid adjustment of root  
299 growth to form of nitrogen source.

300 To explore whether *eir1-4* root growth adapts to different forms of N, elongation  
301 patterns of epidermal and cortex cells were analyzed. Measurements of cell lengths along the  
302 longitudinal growth axis of *eir1-4* roots supplied with  $\text{NH}_4^+$  revealed that unlike in Col-0,  
303 epidermal cells undergo gradual, steady elongation growth comparable to that in cortex.  
304 Notably, patterns of cortex and epidermal cell growth in *eir1-4* appear more synchronous than  
305 in wild-type roots on  $\text{NH}_4^+$  (Fig. 4b versus Fig. 1c). In *eir1-4* roots 12 HAT from  $\text{NH}_4^+$  to  $\text{NO}_3^-$   
306 supplemented medium we observed largely synchronized pattern of elongation in both  
307 epidermal and cortex cell files, characterized by gradual, steady increase of cell length similar  
308 to these observed in Col-0 (Fig. 4c and Fig. 1d). Consistently with a more synchronous pattern  
309 of epidermal and cortex cell growth in both N regimes, no significant differences in frequency  
310 of mitotic events between epidermis and cortex were found in *eir1-4* roots on medium supplied  
311 with either  $\text{NH}_4^+$  or  $\text{NO}_3^-$  (Fig. 4d).

312 Overall, loss of PIN2 activity interfered with enhancement of root growth in response  
313 to  $\text{NO}_3^-$  provision and affected the establishment of tissue specific growth patterns typically  
314 adopted by Col-0 roots supplied with different sources of N. Altogether, these results indicate  
315 that PIN2 mediated basipetal auxin transport plays an important function in acquiring distinct  
316 root growth patterns during adaptation to different N sources.

### 317 ***PIN2 delivery to the plasma membrane and polarity is adjusted in response to form of*** 318 ***nitrogen source***

319 To explore the mechanisms underlying PIN2 function in root growth adaptation to different N  
320 sources we examined its expression, abundance at the plasma membrane (PM) and subcellular  
321 trafficking in roots supplied with  $\text{NH}_4^+$  or  $\text{NO}_3^-$ . RT-qPCR analyses of 7 DAG roots grown on  
322  $\text{NH}_4^+$  and transferred to media supplemented with either  $\text{NH}_4^+$  or  $\text{NO}_3^-$  for 1, 6 and 48 hours  
323 did not reveal any significant changes in *PIN2* transcription in any of the tested conditions (Fig.  
324 S6a). Likewise, expression of neither the *PIN2::nlsGFP* nor the *PIN2::GUS* reporter was

325 affected by different N source (Fig. S6b). Interestingly, monitoring of *PIN2::PIN2-GFP*  
326 transgenic seedlings revealed significantly increased abundance of the PM located PIN2-GFP  
327 in epidermal and cortex cells of roots supplied with  $\text{NO}_3^-$  when compared to  $\text{NH}_4^+$  (Fig. 5a).  
328 Furthermore, in cortex cells at the transition zone of  $\text{NO}_3^-$  supplied roots, besides expected  
329 localization at the apical PM<sup>39</sup>, enhanced lateralization of PIN2-GFP to the inner and outer  
330 PMs could be detected (Fig. 5b, Fig. S6d). Immunolocalisation using PIN2-specific antibodies  
331 is fully consistent with the observations of PIN2-GFP and ruled out possible interference with  
332 fluorescence of GFP reporter by different N source (Fig. S7a-c). Hence, substitution of  $\text{NH}_4^+$   
333 by  $\text{NO}_3^-$  seems to affect PIN2 at post-transcriptional rather than at transcriptional level.

334 PIN proteins constantly recycle between the PM and endosomal compartments, thus  
335 their abundance at the PM is largely dependent on a balance between endo- and exocytosis<sup>47,48</sup>.  
336 Hence, we explored whether modulation of PIN2 subcellular trafficking is the mechanism  
337 involved in adjustment of the PIN2 pattern in response to the available N source. In epidermal  
338 cells on  $\text{NH}_4^+$  when compared to  $\text{NO}_3^-$  supplied roots, the ratio between intracellular versus  
339 PM-located PIN2-GFP was shifted in favor of intracellular localization and frequently  
340 endosomal vesicles with PIN2-GFP signal could be detected (Fig. 5c, Supplemental video 3).  
341 This indicates that dynamics of PIN2 subcellular trafficking might be altered on the basis of  
342 the N source. To assess whether in  $\text{NH}_4^+$  versus  $\text{NO}_3^-$  supplied roots, accumulation of PIN2 at  
343 the PM is the result of a changed balance between endo- and exocytosis, we analyzed  
344 *pPIN2::PIN2-Dendra* seedlings. The irreversible photo-conversion of the Dendra  
345 fluorochrome by UV light from its green form to red allowed us to follow the impact of the N  
346 source on the subcellular fate of PIN2. By monitoring the PIN2-Dendra signal after photo-  
347 conversion (red signal) versus the newly synthesized PIN2-Dendra (green signal) in real time  
348 we could evaluate the kinetics of PIN2 internalization from the PM and delivery of the *de novo*  
349 synthesized PIN2-Dendra proteins. We found that the kinetics of the photo-converted PIN2-  
350 Dendra (red signal) at the PM in either  $\text{NH}_4^+$  or  $\text{NO}_3^-$  were not statistically different, indicating  
351 that the internalization of PIN2 is not affected by the N source. Nevertheless, recovery of the  
352 newly synthesized PIN2-Dendra (green signal) was significantly enhanced in  $\text{NO}_3^-$  when  
353 compared to  $\text{NH}_4^+$  supplied roots (Fig. 5d, Fig. S6c). Considering that different sources of N  
354 did not have significant impact on *PIN2* transcription (Fig. S6a), these results suggest that  
355 recycling or secretion of PIN2 to the PM is more promoted in  $\text{NO}_3^-$  supplied roots than in those  
356 on  $\text{NH}_4^+$ . To further examine the impact of N source on the delivery of PIN2 to the PM we  
357 performed Fluorescence Recovery After Photobleaching (FRAP) analyses on the apical  
358 membrane of the cell. Lateral diffusion of PIN proteins at the PM is negligible<sup>49</sup>, thus PIN2-

359 GFP signal recovery after photobleaching can be correlated with the delivery of PIN2 protein  
360 to the PM. In epidermal cells of  $\text{NO}_3^-$  supplied roots PIN2-GFP signal recovered significantly  
361 faster as compared to roots supplied with  $\text{NH}_4^+$  (Fig. 5e), thus strongly suggesting that delivery  
362 of PIN2 towards the PM is differentially regulated by specific forms of N source.

363 Finally, to examine whether the above described different recycling behavior of PIN2 has an  
364 impact on the establishment of its apical polar domain, we performed super-resolution imaging  
365 employing three-dimensional structured illumination microscopy (3D-SIM). In roots  
366 supplemented with either  $\text{NH}_4^+$  or  $\text{NO}_3^-$ , PIN2-GFP accumulated at the apical edge of epidermal  
367 cells to the same level. However, in  $\text{NH}_4^+$  supplemented roots, number of the PIN2-GFP  
368 positive particles decreased with distance from the cell edge significantly more than in roots  
369 supplied with  $\text{NO}_3^-$  (Fig. 5f).

370 In summary, these results suggest that PIN2 subcellular trafficking, and in particular  
371 the delivery of PIN2 to the PM is differentially adjusted according to the N source.

### 372 ***Nitrogen dependent PIN2 phosphorylation fine-tunes intracellular dynamics and membrane*** 373 ***polarity of PIN2***

374 Post-translational modifications including phosphorylation are regulatory cues with significant  
375 impact on the intracellular trafficking and polar membrane localization of PIN proteins<sup>50</sup>.  
376 Phosphoproteome analysis of samples with either  $\text{NH}_4^+$  or  $\text{NO}_3^-$  as their N source revealed that  
377 PIN2 was among the proteins exhibiting an altered pattern of phosphorylation in response to  
378  $\text{NH}_4^+$  (Vega et al.). Ser439 located at the very end of the PIN2 cytoplasmic loop (C-loop), was  
379 identified as a potential target for differential phosphorylation, where a reduction of  
380 phosphorylation in  $\text{NO}_3^-$  conditions was detected compared root supplied with either  $\text{NH}_4^+$  or  
381 KCl (Vega et al.). Multiple sequence alignment revealed that this Ser439 residue is highly  
382 specific to PIN2 (Fig. S6e). Interestingly, amino acid sequence alignment of PIN2 orthologues  
383 indicated that Ser439 is highly conserved in the PIN2 or PIN2-like clade across plant species  
384 including gymnosperms, mono- and dicotyledonous plants (Fig. S6f).

385 To examine a role of this specific, uncharacterized phosphosite in subcellular dynamics  
386 and function of PIN2, we introduced amino acid substitutions S439D and S439A to achieve  
387 either gain- or loss- of phosphorylation status of PIN2, respectively. *PIN2::PIN2<sup>S439D</sup>-GFP* and  
388 *PIN2::PIN2<sup>S439A</sup>-GFP* constructs were introgressed into the *eir1-4* mutant line. The phosphor-  
389 variant version PIN2<sup>S439D</sup>-GFP, like PIN2-GFP, accumulated at the PM of epidermal and cortex  
390 cells significantly more in roots supplied with  $\text{NO}_3^-$  than  $\text{NH}_4^+$  (Fig. 6a, b, d). Interestingly, the  
391 amount of the PM localized phospho-dead PIN2<sup>S439A</sup>-GFP in  $\text{NH}_4^+$  -supplied roots was

392 significantly higher when compared to PIN2-GFP and PIN2<sup>S439D</sup>-GFP, and only a slight  
393 increase in epidermal cells could be detected in response to NO<sub>3</sub><sup>-</sup> supply (Fig. 6a, c, d).  
394 Furthermore, in cortex cells at the TZ, reduced lateralization of PIN2<sup>S439D</sup>-GFP on NO<sub>3</sub><sup>-</sup>  
395 supplemented medium could be observed. PIN2<sup>S439A</sup>-GFP lateralized towards outer and inner  
396 PMs irrespective of the N source thus phenocopying the PIN2-GFP pattern in NO<sub>3</sub><sup>-</sup> supplied  
397 roots (Fig. 6e-g). Altogether, these results suggest that phosphorylation status of PIN2 on S439  
398 account for fine-tuning of PIN2 trafficking towards the PM and polarity establishment under  
399 varying N sources.

#### 400 ***Nitrogen dependent PIN2 phosphorylation fine-tunes PIN2 mediated root growth***

401 Next, we examined the impact of PIN2 phosphorylation status on the root growth adaptations  
402 to different N source. To evaluate functionality of PIN2-GFP constructs with phosphosite  
403 substitutions, we analyzed their ability to rescue the agravitropic phenotype of *eir1-4*.  
404 *PIN2::PIN2<sup>S439D</sup>-GFP* as well as *PIN2::PIN2<sup>S439A</sup>-GFP* constructs were able to rescue the  
405 agravitropic phenotype of the *eir1-4* mutant (Fig. S8a), indicating that the overall activity was  
406 maintained in both mutated variants. However, measurements of roots 6, 24 and 96 HAT on  
407 either NH<sub>4</sub><sup>+</sup> or NO<sub>3</sub><sup>-</sup> supplemented media revealed that modulation of PIN2 phosphorylation  
408 status interfere with the flexible adjustment of root growth to N source. Roots of  
409 *PIN2::PIN2<sup>S439D</sup>-GFP;eir1-4* exhibited enhanced growth already 6 hours after transfer on NO<sub>3</sub><sup>-</sup>  
410 when compared to NH<sub>4</sub><sup>+</sup> supplemented medium (Fig. 7a); however, when compared to control  
411 seedlings the enhancement of root growth by NO<sub>3</sub><sup>-</sup> was less pronounced 4 DAT (Fig. S8b).  
412 This suggests that PIN2<sup>S439D</sup>-GFP is partially able to mediate distinct root growth responses to  
413 different N sources. Roots of *eir1-4* expressing *PIN2::PIN2<sup>S439A</sup>-GFP* exhibited delay in  
414 adjusting growth to NO<sub>3</sub><sup>-</sup> provision and no significant increase in length 6 and 24 HAT to NO<sub>3</sub><sup>-</sup>  
415 when compared to NH<sub>4</sub><sup>+</sup> could be detected (Fig. 7a; S8b).

416 Intriguingly, although *PIN2::PIN2<sup>S439D</sup>-GFP* partially recovered the ability of *eir1-4*  
417 roots to adjust elongation growth to N source, in depth analysis of epidermal and cortex cell  
418 files revealed intriguing differences when compared to control roots. In *PIN2::PIN2<sup>S439D</sup>-*  
419 *GFP;eir1-4* roots, irrespective of the N source, length of epidermal cells steeply increased with  
420 distance from QC, whereas cortex cells underwent slow steady elongation. Similar  
421 asynchronous growth patterns in epidermal and cortex cell files were observed in NH<sub>4</sub><sup>+</sup>, but  
422 not in NO<sub>3</sub><sup>-</sup> supplied *PIN2::PIN2-GFP;eir1-4* and Col-0 roots, indicating that  
423 *PIN2::PIN2<sup>S439D</sup>-GFP* is not able to recover all aspects of root adaptation to varying N supply  
424 (Fig. 7b,c compared to Fig. S8c, Fig.1c). In *PIN2::PIN2<sup>S439A</sup>-GFP* roots irrespective of the N



425 source, shallow slope of epidermal cell length was detected, which resulted in synchronized  
426 growth patterns of epidermal and cortex cell files, resembling those observed in *PIN2::PIN2-*  
427 *GFP,eir1-4* and Col-0 roots supplied with  $\text{NO}_3^-$  (Fig. 7d, e compared to Fig. S8c, Fig.1d). Thus,  
428 *PIN2::PIN2<sup>S439A</sup>-GFP, eir1-4* roots supplemented with  $\text{NH}_4^+$  acquired features typical for Col-  
429 0 roots supplied with  $\text{NO}_3^-$ .

430 In summary, the *PIN2<sup>S439D</sup>-GFP* phospho-variant is lacking the enhanced elongation  
431 growth of *eir1-4* roots, but it is unable to synchronize the patterns of epidermis and cortex  
432 elongation in response to  $\text{NO}_3^-$ . Unlike *PIN2<sup>S439D</sup>-GFP*, *PIN2<sup>S439A</sup>-GFP* is unable to rescue  
433 sensitivity of *eir1-4* roots to  $\text{NO}_3^-$  stimulatory effect on root elongation growth and to  
434 synchronize the patterns of epidermis and cortex elongation growth, irrespective of N source.  
435 Taking together, these results indicate that N dependent regulation of phosphorylation status  
436 of PIN2 at S439 is a part of complex mechanism underlying root growth adaptation to specific  
437 N source, which involves coordination of tissue specific balance between cell proliferation and  
438 elongation.

439 ***An experimentally-derived quantitative model predicts nitrogen-dependent coordination of***  
440 ***root growth***

441 Experimental findings suggest that nitrogen-dependent fine-tuning of polar auxin transport  
442 through the regulation of PIN2 phosphorylation status could coordinate the growth of adjacent  
443 tissues and thereby steer the root growth. To mechanistically understand nutrient effect on plant  
444 root growth, we developed a multilevel computer model of epidermis and cortex tissues. The  
445 complete scheme of the model components can be found in Fig. S9 and a full description of  
446 the model is provided in the Methods section. The model integrates the experimental  
447 observations of N source dependent effects on PIN2 accumulation at the PM (Supplementary  
448 dataset 1) and previously shown auxin-dependent degradation of *PIN2<sup>S439D</sup>*<sup>51,52</sup>. As a source of  
449 auxin we tested two likely scenarios *i.*) a uniform source of auxin along the epidermis (Model  
450 A) or *ii.*) flow of auxin from lateral root cap (LRC) and QC into epidermis<sup>53,54</sup> (Model B). In  
451 addition, other less favorable scenarios were also tested (see Methods and Fig. S10f).  
452 Importantly, PIN2 polarity and auxin distribution as well as cell length and number of cell  
453 division resulted purely from predictions of the model. To test our models, we compared  
454 experimental observations of PIN2 distributions (Supplementary Video 6, Supplementary data  
455 set 1), cell length measurements (Fig. 1, Supplementary dataset 1) and auxin content (Fig. 2,  
456 Supplementary data set 1) with the predicted by computer model simulations. The initial Model  
457 A failed to recapitulate experimental data (Fig. S10b-d), indicating that the auxin source



458 assumption may not be correct and/or there are missing components, which were not  
459 considered in this model. Model B, which unlike Model A, integrates flow of auxin from the  
460 QC and the LRC into the epidermis, and in addition, it implements correlation between cell  
461 distance from the QC with both increased PIN2 trafficking and PIN2 degradation (Fig. S10e),  
462 was able to recapitulate PIN2 and auxin distributions as well as cell length across the meristem  
463 (Supplementary Fig.10a-d and 10f). To comprehend a necessity for these two essential  
464 components in our model, we closely inspected the relation between auxin activity levels and  
465 PIN2 fluorescence in our experimental dataset in roots supplemented with  $\text{NO}_3^-$  or  $\text{NH}_4^+$ . Our  
466 analysis revealed that for the same auxin activity two different PIN2 levels were observed in  
467 both the cortex and the epidermis that was dependent on distance from the QC - a component  
468 missing in Model A (Fig. S10a). This eminently bi-stable feature was important to guarantee  
469 the synchrony of cell elongation between adjacent tissues as this feature was compromised in  
470  $\text{NH}_4^+$  grown roots that showed an asynchronous elongation of adjacent cortex and epidermal  
471 cells (Fig. S10a). Notably, Model B could successfully capture this relation (Fig. S10c, d).  
472 Finally, we coupled auxin activity to cell division and elongation and simulated our root model  
473 in both  $\text{NH}_4^+$  and  $\text{NO}_3^-$  regimes (Fig. 8b). As for previous simulations, the computer model of  
474 root growth does not include neither fixed auxin levels nor pre-patterned PIN2 polarization and  
475 was capable of recapitulating *in planta* root growth patterns in those different N sources (Fig.  
476 8b, Supplementary Videos 7 and 8). Furthermore, model predictions such as lateral auxin  
477 distribution (Fig. 8c), meristem length (Fig. 8d) and proliferation dynamics (Fig. 8e) are in a  
478 fair agreement with experimental results (Figs. 1 and 2). Importantly, our model predicts  
479 mechanistic principles of the growth in synchrony such as coordinated cell divisions in both  
480 epidermis and cortex tissues further away from QC (Fig. 8e) and lateral auxin transport through  
481 PIN2 between cortex and epidermis near the transition zone (Fig. 8c).  
482 Mechanisms that trigger the transition from meristematic activity to cell elongation are not well  
483 understood<sup>55</sup>. Auxin plays a fundamental role in the establishment of the TZ<sup>56,57</sup>. Our model  
484 could predict a precise threshold of auxin levels that was necessary to determine the transition  
485 to elongation. This auxin threshold is dynamic as it depends on the actual N source; in  
486 particular, higher levels of auxin were required to advance cell elongation on  $\text{NO}_3^-$  (Fig. 8f).  
487 Taken together, we have developed a quantitative experimentally-supported computer model  
488 of root growth in different N sources that was capable of recapitulating all experimental  
489 observations as well as generating new predictions that could broaden our understanding of  
490 root growth mechanisms in the dynamic environment.

## 491 Discussion

492 Ammonium and nitrate represent major inorganic forms of N absorbed by plants. Since the  
493 distribution of these N sources in the soil is very heterogeneous<sup>58</sup>, plants tend to maximize the  
494 N exploitation by flexible modulation of root system architecture<sup>59</sup>. Although distinct impacts  
495 of  $\text{NH}_4^+$  and  $\text{NO}_3^-$  on the root system growth and development have been already  
496 demonstrated<sup>6</sup>, molecular mechanisms how spatio-temporal changes in N resource impact on  
497 root growth are scarcely described.

498 Root growth is determined by the production of new cells at the apical meristem and  
499 their rapid elongation need to be well coordinated across diverse cell types of the root organ.  
500 Conversion from proliferative to elongation phases occurs as cells pass through the TZ where  
501 they undergo complex cyto-architectural re-arrangement<sup>57</sup>. Hence, alterations of root growth  
502 kinetics might result from modulation of any of these growth-determining processes. We show  
503 that replacement of  $\text{NH}_4^+$  for  $\text{NO}_3^-$  has a rapid impact on root growth kinetics and in particular  
504 progression of cells through individual root zones. While in roots supplied with  $\text{NH}_4^+$ ,  
505 proliferative capacity of epidermal cells is attenuated in closer distance to the QC, which led  
506 to their earlier and rapid transition to elongation phase when compared to cortex, provision of  
507  $\text{NO}_3^-$  promotes proliferation and steady elongation of epidermal cells, which results in well-  
508 synchronized growth patterns of epidermis and cortex. Hence, adaptation of primary roots to  
509 different sources of N encompass a tissue specific modulation of cell proliferation and cell  
510 growth kinetics.

511 Auxin is an essential patterning cue during plant growth and development. A number  
512 of recent studies have demonstrated that levels and distribution of this hormone have instructive  
513 function in many aspects of root growth including the root apical meristem patterning, its size  
514 determination, transition of meristematic cells into the elongation phase and capacity of cells  
515 to elongate<sup>55,60,61</sup>. Whereas the exit of cells from meristematic zone was associated with local  
516 auxin minima that has been proposed to define the transition zone<sup>60</sup>, increase of auxin signaling  
517 along the longitudinal root growth axis correlated with cell wall acidification as a potential  
518 driving force of cell elongation<sup>62</sup>.

519 Experimental measurements supported by a quantitative computational model indicate  
520 that adjustment of root growth dynamics in different N regimes is dependent on the precise  
521 modulation of auxin transport routes between cortex and epidermis. The steep increase of auxin  
522 activity correlating with earlier attenuation of proliferation activity in the epidermis and  
523 transition of cells into the elongation phase was eminent in roots grown on  $\text{NH}_4^+$ . In contrast,

524 shallow slopes of the auxin activity in both epidermis and cortex corresponded with delayed,  
525 gradual transition of epidermal cells into elongation phase in roots supplemented with  $\text{NO}_3^-$ ,  
526 showing a tight growth synchronization with adjacent cortex tissues. Based on these  
527 observations we demonstrate that a flexible modulation of auxin activity in response to varying  
528 sources of N is largely consistent with described impact of auxin on key events defining root  
529 growth such as transition into elongation growth and kinetics of elongation.

530 Delivery of auxin in outer tissues including the cortex and the epidermis is largely  
531 mediated by the PIN2 auxin efflux carrier<sup>43,44</sup>. While PIN2 dependent basipetal transport of  
532 auxin is instructive for elongation growth and root gravity bending<sup>63</sup>, PIN2 mediated reflux to  
533 inner tissues has been associated with maintenance of root meristem size<sup>39</sup>. Measurements of  
534 the auxin transport revealed that replacement of  $\text{NH}_4^+$  by  $\text{NO}_3^-$ , significantly enhances flow of  
535 auxin in the basipetal direction which correlates with increased PIN2 activity near the transition  
536 zone. Loss of PIN2 activity not only interferes with the  $\text{NO}_3^-$  stimulated transport of auxin  
537 towards the shoot, but also severely affects adaptive responses of roots to this N source.  
538 Furthermore, model predictions based on these experimental measurements suggest a bi-stable  
539 relationship between auxin levels and PIN2 activity and cell elongation that is enhanced in  
540  $\text{NO}_3^-$ , which could explain why roots grown on nitrate can coordinate their growth by passing  
541 auxin between cortex and epidermal cells in a synchronous manner. Furthermore, our model  
542 confirmed the necessity for self-emerging communication between cortex and epidermis via  
543 auxin with quantitative computer simulations of root growth under different N conditions.

544 Dynamic, N source dependent accumulation and polarization of PIN2 at the PM, but  
545 unchanged *PIN2* transcription, pointed at post-transcriptional regulatory mechanism  
546 underlying adaptation of basipetal auxin transport to N supply. Replacement of  $\text{NH}_4^+$  by  $\text{NO}_3^-$   
547 promoted accumulation of PIN2 at the apical PM of epidermal and cortex cells as well as to  
548 the lateral sides.

549 Phosphorylation has been recognized as a prominent posttranslational modification of  
550 PIN proteins that determines their polar membrane localization and activity<sup>64</sup>. Unexpectedly,  
551 genome-wide analysis of the phosphoproteome during early phases of root adaptation to  
552 provision of  $\text{NO}_3^-$  (Vega et al.) retrieved PIN2 among differentially phosphorylated proteins.  
553 Serine 349 of PIN2 in *Arabidopsis*, found to undergo a rapid de-phosphorylation after  
554 replacement of  $\text{NH}_4^+$  by  $\text{NO}_3^-$ . The PIN2S439 phosphosite was not completely unknown: it was  
555 originally identified as differentially phosphorylated during lateral root morphogenesis<sup>65</sup>. It is  
556 positioned in the hydrophilic loop domain of the PIN2 protein and is an evolutionarily  
557 conserved residue in the PIN2 or PIN2-like clade across species including gymnosperms,

558 mono- and dicotyledonous plants, suggesting that PIN2 might be universally involved in other  
559 plant species adaption strategies to the changing N sources by means of its post-translational  
560 (phosphorylation) mechanism. The functional characterization of PIN2 and its phosphor-  
561 variants suggests that N source dependent regulation of PIN2 phosphorylation status has a  
562 direct impact on the flexible adjustment of PIN2 membrane localization and polarity, and  
563 thereby adaptation of root growth to varying forms of N supply.

564

## 565 **Acknowledgments**

566 We acknowledge Gergely Molnár for critical reading of the manuscript, Alexander Johnson  
567 for language editing and Yulija Salanenka for technical assistance. Work in the Benková lab  
568 was supported by the Austrian Science Fund (FWF01\_I1774S) to KÖ and EB. Work in the  
569 Wabnik lab was supported by the Programa de Atracción de Talento 2017 (Comunidad de  
570 Madrid, 2017-T1/BIO-5654 to K.W.), Severo Ochoa Programme for Centres of Excellence in  
571 R&D from the Agencia Estatal de Investigación of Spain (grant SEV-2016-0672 (2017-2021)  
572 to K.W. via the CBGP) and Programa Estatal de Generación del Conocimiento y  
573 Fortalecimiento Científico y Tecnológico del Sistema de I+D+I 2019 ( PGC2018-093387-A-  
574 I00 ) from MICIU (to K.W.)

575 We acknowledge the Bioimaging Facility in IST-Austria and the Advanced Microscopy  
576 Facility of the Vienna BioCenter Core Facilities, member of the Vienna BioCenter Austria, for  
577 use of the OMX v4 3D SIM microscope. AJ was supported by the Austrian Science Fund  
578 (FWF): I03630 to J.F.

579

## 580 **Author Contributions**

581 K.Ö. and E.B. conceived the project; K.Ö. performed most of the experiments; M.M.  
582 contributed to the generation of the computational model; A.V., J.B. and R.G. shared  
583 unpublished material; A.J. performed the 3D-SIM experiment; R.A. performed q-PCR and  
584 GUS-staining experiments; L.A. performed the regression analysis; J.C.M. contributed to the  
585 multiphoton microscopy imaging; Y.Z. conducted protein sequence alignments; S.T. generated  
586 the DII and mDII lines in the *eir1-4* background; C.C., El.B. and A.G. designed and performed  
587 some of the pre-pilot experiments; C.A. assisted K.Ö. in multiple experiments; J.F. financially  
588 supported A.J., Y.Z. and S.T. The manuscript was written by K.Ö., K.W. and E.B.

589

## 590 **Corresponding authors**

591 Correspondence to Krzysztof Wabnik and Eva Benková.

592

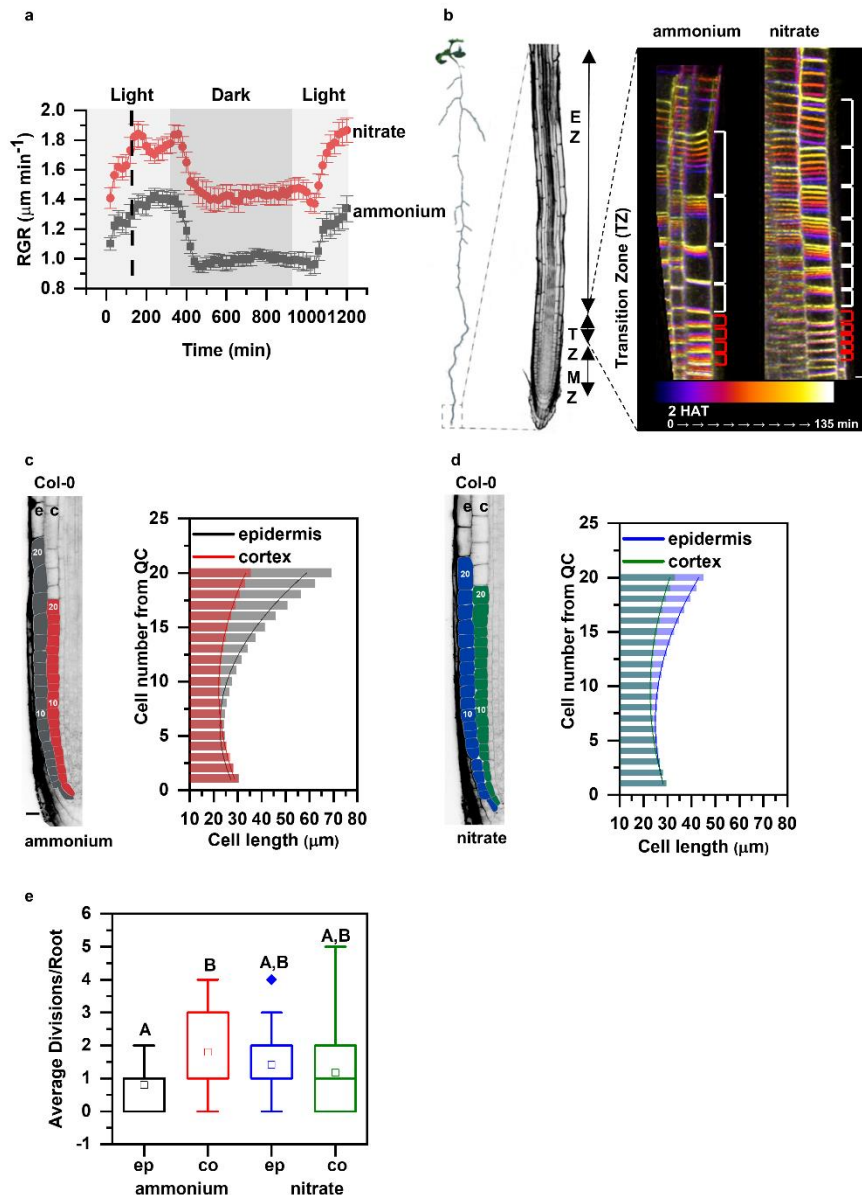
593 **Competing interests**

594 The authors declare no competing interests.

595

596 **Figures**

597



598

599 **Figure 1. Primary root growth kinetics of *Arabidopsis thaliana* (*L.*) *Heynh.***

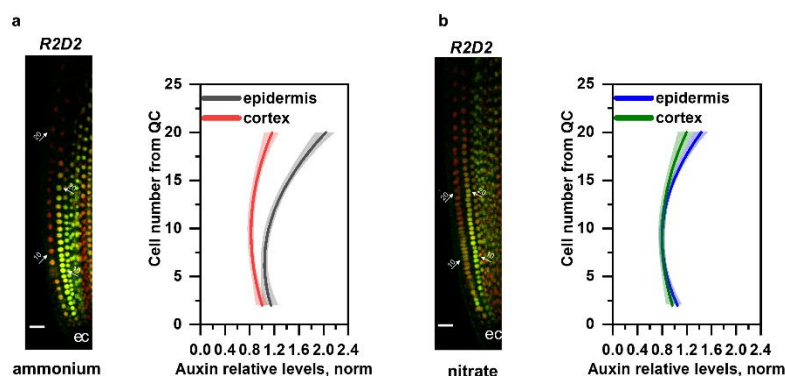
600 *Columbia-0*, Col-0) on ammonium or nitrate containing medium. **a.** Seedlings were

601 transferred 5 days after germination (DAG) to medium supplemented with ammonium (grey)

602 or nitrate (red). Root growth rates (RGR in  $\mu\text{m}/\text{min}$ ) were monitored over a 1200 minutes

603 period. Data represent the geometric mean ( $\pm$  standard error, SE) of three independent

604 experiments (each consisting of 3 roots per treatment). Light and dark periods are indicated as  
605 light or dark gray background, respectively. **b.** On the left, schematic representation of distinct  
606 root zones: Meristematic Zone (MZ), Transition Zone (TZ) and Elongation Zone (EZ). On the  
607 right, time lapse imaging of cell growth at the TZ. Cells were visualized using the plasma  
608 membrane marker (wave line W131Y). Observation of roots started 2 hours after transfer (2  
609 HAT; blue) on ammonium or on nitrate for 135 min (white) and images were recorded every  
610 20 minutes (9 stacks/root/recording). Red and white brackets indicate the length of  
611 meristematic and elongating cells at the last measurement point, respectively. Scale bar = 30  
612  $\mu\text{m}$ . **c and d.** Representation and quantification of cell length in epidermal (e) and cortical (c)  
613 cell files. Optical, longitudinal sections of 5 DAG old Col-0 roots 12 HAT to ammonium (C)  
614 or nitrate (D) supplemented media. The first 20 epidermal (e) and cortex (c) cells (from  
615 quiescent center (QC)) are highlighted in grey and in red on ammonium (C), and in blue and  
616 green on nitrate (D), respectively. Scale bar = 30  $\mu\text{m}$ . Column bars denote the geometric mean  
617 of the cell lengths at the respective positions. Lines represent a polynomial regression fit, with  
618 calculated slopes between cells 10 and 20 of  $3.32639 \pm 0.17172$  (ammonium, epidermis),  
619  $1.22033 \pm 0.08754$  (ammonium, cortex) and  $1.70502 \pm 0.09532$  (nitrate, epidermis),  
620  $0.82342 \pm 0.06973$  (nitrate, cortex). Data are derived from 3 independent experiments; total  
621 number of analyzed roots are  $n=18$  in each case. **e.** Graphical representation of the average  
622 number of cell divisions along epidermis (ep) and cortex (co) in 5 DAG root tips 12 HAT to  
623 ammonium or nitrate supplemented media. Data are derived from 15 and 17 roots. The  
624 statistical significance was evaluated with ANOVA at  $p < 0.05$ .

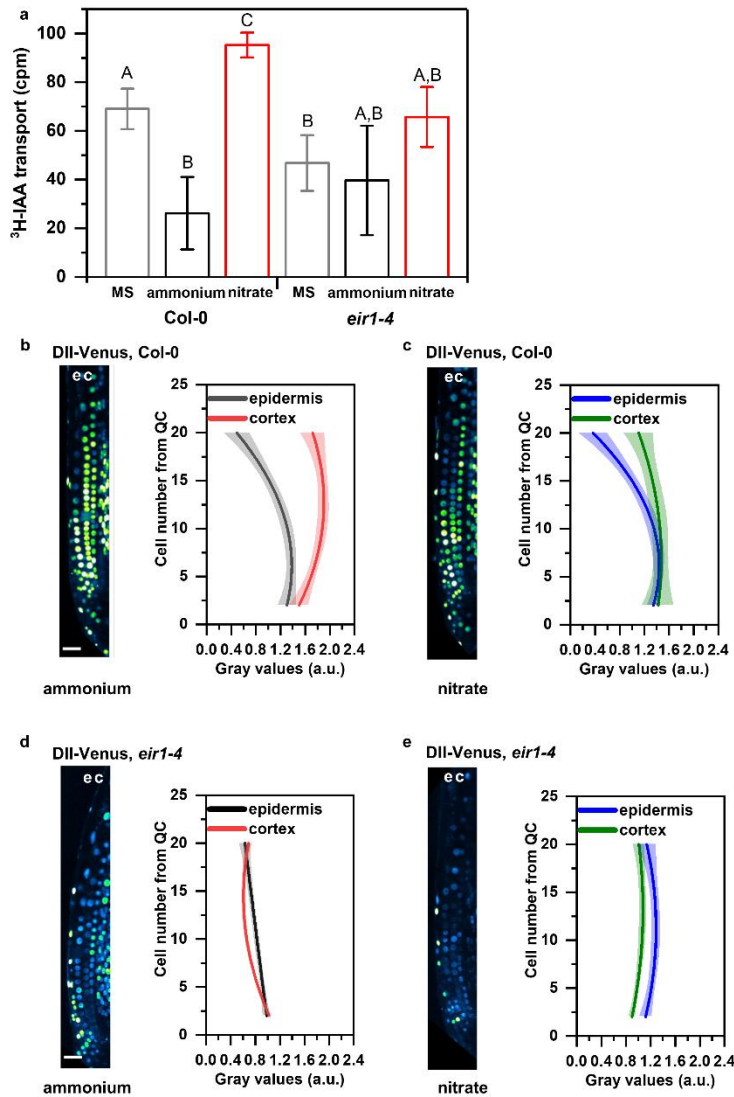


625

626 **Figure 2. Relative auxin level in Col-0 root tips transferred to medium supplemented with**  
627 **ammonium or nitrate.** Maximum intensity Z-stack projection images of 5 DAG old roots  
628 expressing the *R2D2* auxin signaling reporter 12 HAT to ammonium (a) or nitrate (b)  
629 supplemented media. White arrows mark the position of the 10<sup>th</sup> and 20<sup>th</sup> cells from QC; “e”



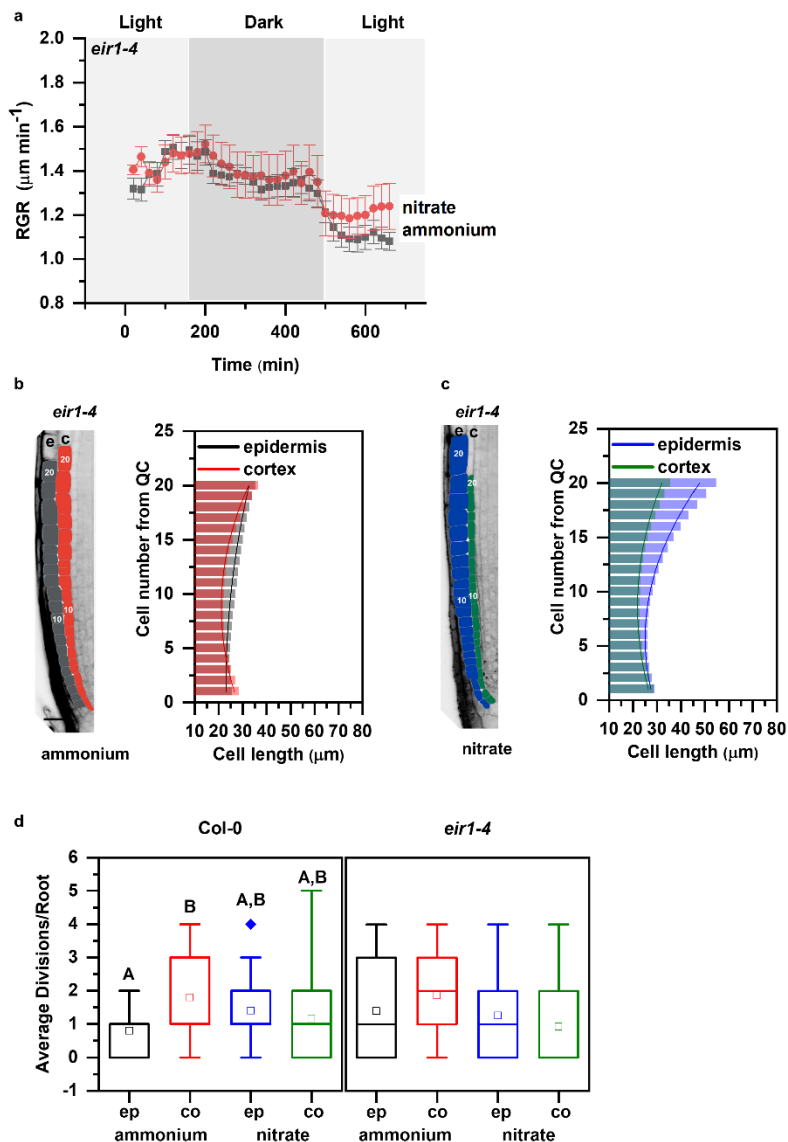
630 and “c” mark epidermis and cortex, respectively. Scale bar = 50  $\mu$ m. Graphs denote normalized  
 631 relative auxin levels at the respective positions. Lines represent polynomial regression fit with  
 632 95% confidence band. Data are derived from 5 roots per condition from three independent  
 633 experiments.



634

635 **Figure 3. Monitoring basipetal auxin transport and auxin response at root tips of Col-0**  
 636 **and *eir1-4* roots transferred to ammonium or nitrate containing medium. a.** Basipetal  
 637 (shootward) auxin transport measurements in Col-0 and *eir1-4* roots grown on control  
 638 Murashige and Skoog (MS) or with either nitrate or ammonium supplied media.  $^3\text{H-IAA}$  was  
 639 applied at the root tip of 7 DAG wild-type (Col-0) or *eir1-4* seedlings. Radioactivity was  
 640 measured 6 h after application of  $^3\text{H-IAA}$  in root segments after excision of the apical  $\approx$  1 mm  
 641 of the root tip. Values shown are the geometric mean ( $\pm$  standard error, SE) for at least 30  
 642 seedlings. The amount of auxin transported into each root segment for Col-0 and *eir1-4* was

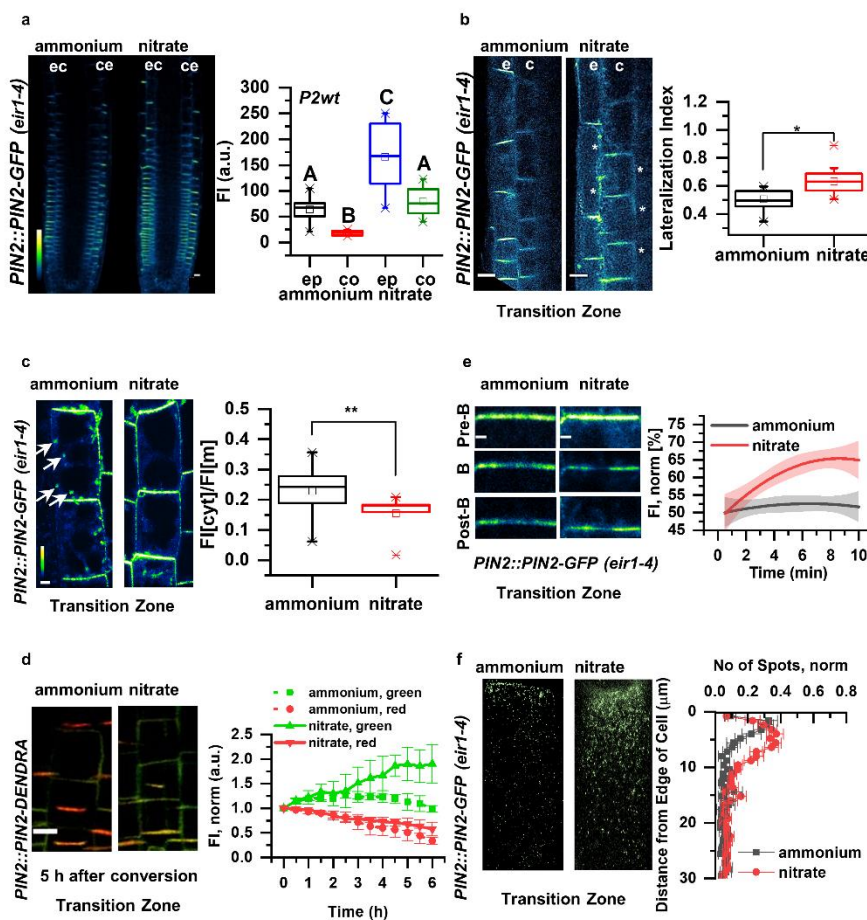
643 compared by ANOVA at  $p < 0.05$ . cpm, counts per minute. **b-e**. Maximum intensity Z-stack  
644 projection images of 5 DAG old Col-0 and *eir1-4* roots expressing the *DII-Venus* auxin  
645 signaling reporter 12 HAT to ammonium (**b and d**) or nitrate (**c and e**) supplemented media.  
646 “e” and “c” mark epidermis and cortex, respectively. Scale bar = 50  $\mu\text{m}$ . Graphs denote  
647 normalized relative auxin levels at the respective positions. Lines represent polynomial  
648 regression fit with 95% confidence band. Data are derived from measurements of  $n=8$   
649 (ammonium) and  $n=10$  (nitrate) roots of Col-0 and  $n=10$  roots of *eir1-4* per condition.



650

651 **Figure 4. Primary root growth kinetics of *eir1-4* roots transferred to ammonium or**  
652 **nitrate amended medium. a.** Root growth rate (RGR in  $\mu\text{m}/\text{min}$ ) of *eir1-4* roots transferred 5  
653 DAG to ammonium (grey) or nitrate (red) containing medium over a period of 680 minutes.  
654 Data represent the geometric mean ( $\pm$  standard error, SE) of three independent experiments  
655 (number of roots  $n=5$  in each case). Light and dark periods are highlighted in light or dark gray.

656 **b and c.** Representation and quantification of cell length in epidermal (e) and cortical (c) cell  
 657 files. Optical, longitudinal sections of 5 DAG *eir1-4* roots 12 HAT to ammonium (B) or nitrate  
 658 (C) supplemented media. The first 20-20 epidermal and cortex cells (from quiescent center  
 659 (QC)) are highlighted in grey and in red on ammonium (B) and in blue and green on nitrate  
 660 (C), respectively. Scale bar = 30  $\mu$ m. Column bars denote the geometric mean of cell length at  
 661 the respective positions. Lines represent a polynomial regression fit, with calculated slopes  
 662 between cells 10 and 20 of  $0.75884 \pm 0.02624$  (ammonium, epidermis),  $1.13088 \pm 0.08446$   
 663 (ammonium, cortex) and  $2.06912 \pm 0.10341$  (nitrate, epidermis),  $0.99878 \pm 0.07278$  (nitrate,  
 664 cortex). Data are derived from 3 independent experiments, total number of the analyzed roots  
 665 are  $n=9$ , ammonium and  $n=8$ , nitrate. **d.** Average number of cell divisions along the epidermis  
 666 (ep) and cortex (co) in 5 DAG old Col-0 and *eir1-4* root tips 12 HAT to ammonium or nitrate  
 667 supplemented media. Data are derived from  $n=15$  and  $n=17$  roots of Col and  $n=10$  and  $n=9$   
 668 roots of *eir1-4* on ammonium and nitrate, respectively. Statistical significance was evaluated  
 669 with ANOVA at  $p < 0.05$ .

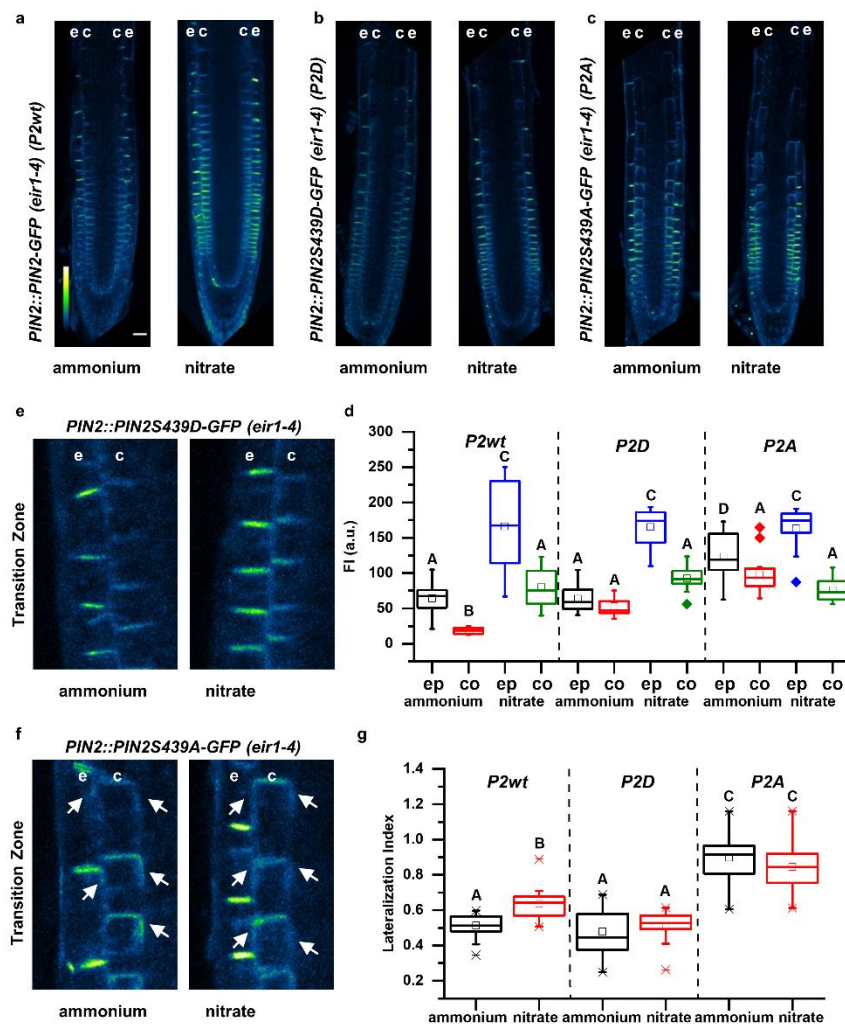


670

671 **Figure 5. PIN2 protein abundance, polarity and vacuolar trafficking in roots on**  
 672 **ammonium or nitrate containing medium. a.** Pseudo-colored, optical longitudinal cross

673 sections of 5 DAG roots expressing *PIN2::PIN2-GFP*, *eir1-4* 12 HAT to ammonium or nitrate  
674 supplemented media. “e” denotes epidermis and “c” cortex, respectively. Color code represents  
675 GFP intensity from low (blue) to high (white) values. Scale bar = 20  $\mu$ m. Box plots display the  
676 distribution of the cell membrane derived PIN2-GFP fluorescence intensity (FI) values (in  
677 arbitrary units, a.u.) on ammonium (grey, epidermis (ep) and red, cortex (co), n=15) and nitrate  
678 (blue, epidermis (ep) and green, cortex (co), n=10) grown roots. 5 cells per root were analyzed.  
679 The statistical significance was evaluated with ANOVA at  $p < 0.05$ . **b.** Higher magnification of  
680 pseudo-colored confocal images of 5 DAG old roots expressing PIN2-GFP 12 HAT to  
681 ammonium or nitrate supplemented media. “e” denotes epidermis and “c” cortex, respectively.  
682 Color code represents GFP intensity from low (blue) to high (white) values. Scale bar = 12  $\mu$ m.  
683 White stars mark PIN2-GFP protein localization on the lateral membranes. Box plots display  
684 lateralization index (fluorescent signal detected on apical/basal membranes divided by the  
685 signal value at inner/outer membranes) of roots on ammonium (n=31 cells from 6 roots) or  
686 nitrate (n=24 cells from 6 roots) supplemented medium. **c.** Pseudo-colored PIN2-GFP signal  
687 in epidermal cells of 5 DAG old roots 12 HAT to ammonium or nitrate containing media. White  
688 arrows point to PIN2-GFP containing intracellular vesicles. Box plots represent the ratio in  
689 fluorescent signal detected inside the cell vs on the membranes (FI[cyt]/FI[m]). n=6 roots per  
690 condition, 5 cells per root analyzed. Scale bar = 5  $\mu$ m. **e.** FRAP analysis of PIN2 protein  
691 mobility in *PIN2::PIN2-GFP* expressing epidermal cells 12 HAT to ammonium or nitrate. The  
692 graph shows polynomial regression fit with 95% confidence band of the mean signal recovery  
693 in the bleached region of interest (ROI) after background subtraction and normalization to  
694 photobleaching. Data are derived from 3 independent experiments, each consisting of 5  
695 membranes from 3 different roots. Scale bar = 2  $\mu$ m. **d.** Microscopic images showing PIN2-  
696 Dendra fluorescent signal five hours after photoconversion of PIN2-Dendra into its red form.  
697 Depletion of the red signal and recovery of the green signal over a 6 hours period was followed  
698 in parallel in 5 DAG old roots 12 HAT to ammonium or nitrate supplemented media. Note the  
699 increase in the intensity of the green signal in roots transferred to nitrate. Graph represents the  
700 mean signal  $\pm$  SD (n=6 roots per condition, 20 cells per root analyzed). The experiment was  
701 repeated 3 times. Scale bar = 20  $\mu$ m. **f.** Representative 3D SIM microscopic images of 10 DAG  
702 old epidermal cells expressing *PIN2-GFP* 12 HAT to ammonium or nitrate containing media.  
703 Green dots represent PIN2-GFP on the lateral cell surface (polar domain) of epidermal cells in  
704 the transition zone. Graph represents the number of GFP positive spots along a 30  $\mu$ m long  
705 region starting at the apical side of the cell (8 cells per 4 roots and 9 cells per 4 roots) were

706 analyzed per treatment, experiment was done 3 times. Note the effect of ammonium versus  
 707 nitrate on the distribution of the PIN2-GFP spots.

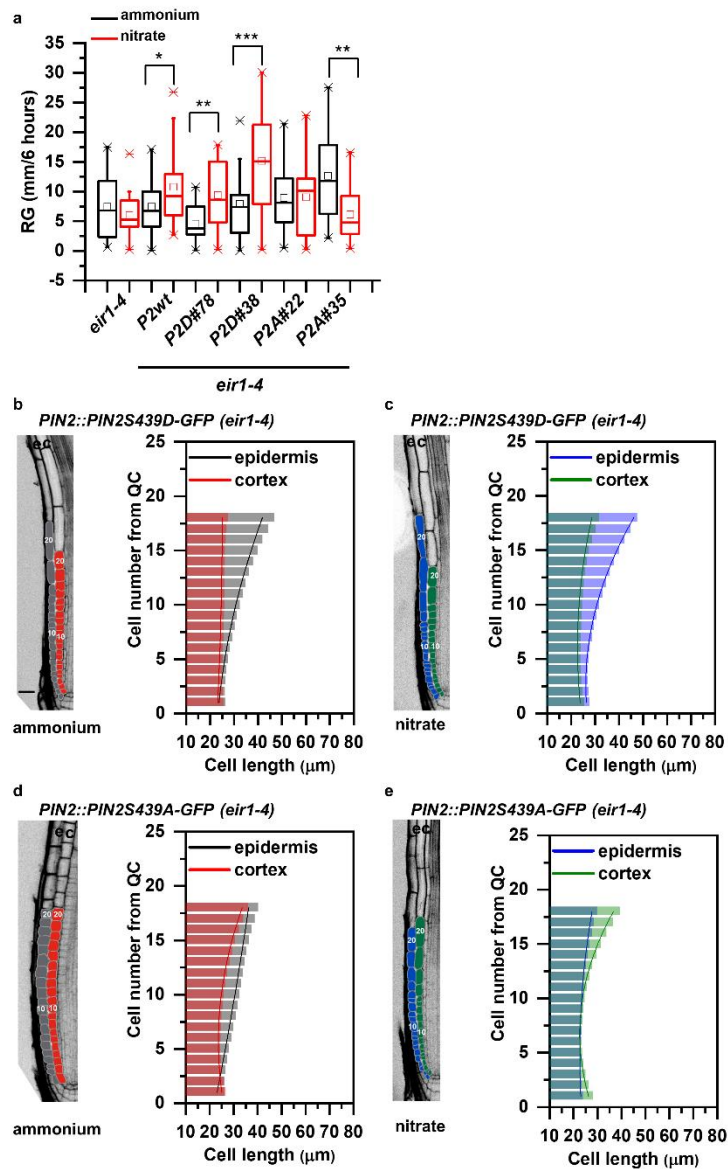


708

709 **Figure 6. Impact of Ser439 on PIN2 localization in roots supplemented with ammonium**  
 710 **or nitrate. a - c.** Pseudo-colored, optical longitudinal cross sections of 5 DAG roots expressing  
 711 (a) *PIN2-GFP* (*PIN2::PIN2-GFP*, *P2wt*) (b) *PIN2S439D-GFP* (*PIN2::PIN2S439D-GFP*,  
 712 *P2D*) and (c) *PIN2S439A* (*PIN2::PIN2S439A-GFP*, *P2A*) - all in *eir1-4* background – 12 HAT  
 713 to ammonium or nitrate supplemented media. “e” denotes epidermis and “c” cortex,  
 714 respectively. Color code represents GFP intensity from low (blue) to high (white) values. Scale  
 715 bar = 50  $\mu$ m. **d.** Box plots display the distribution of the cell membrane derived PIN2-GFP  
 716 fluorescence intensity (FI) values (in arbitrary units, a.u.) in roots transferred to ammonium  
 717 ((grey, epidermis (ep) and red, cortex (co) and to nitrate (blue, epidermis (ep) and green, cortex  
 718 (co)). 5 cells per roots were analyzed in at least 9 roots per genotype per treatment. The  
 719 statistical significance was evaluated with ANOVA at  $p < 0.05$ . **e and f.** Microscopic images of  
 720 5 DAG old roots expressing (e) *PIN2::PIN2S439D-GFP* and (f) *PIN2::PIN2S439A-GFP*



721 HAT to ammonium or nitrate amended media. “e” denotes epidermis and “c” cortex,  
 722 respectively. White arrows point to PIN2-GFP protein localization on the lateral membranes.  
 723 **g.** Box plots display lateralization index (fluorescent signal detected on apical/basal membranes  
 724 vs inner/outer membranes) of *P2wt*, *P2D* and *P2A* roots transferred to ammonium (grey) or  
 725 nitrate (red) supplemented medium. At least 24 cells from 5 roots were analyzed per genotype  
 726 per treatment. The statistical significance was evaluated with ANOVA at  $p < 0.05$ .

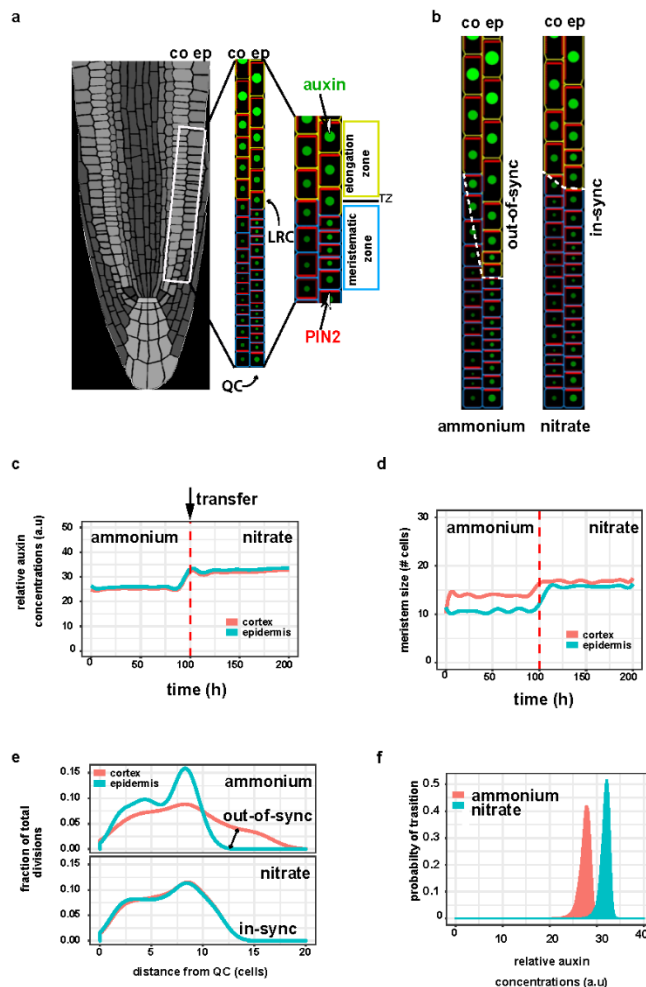


727

728 **Figure 7. Impact of PIN2S439 phospho-variants on the adaptation of the primary root**  
 729 **growth to ammonium or nitrate provision.** **a.** Box plot representation of root growth (μm/6  
 730 hours) of *eir1-4*, Col-0, *PIN2::PIN2-GFP* (*P2wt*), two independent *PIN2::PIN2S439D-GFP*  
 731 (*P2D*) lines (#78 and #38) and two independent *PIN2::PIN2S439A-GFP* (*P2A*) lines (#22 and  
 732 #35) transferred to ammonium or nitrate containing medium. At least 10 roots were analyzed

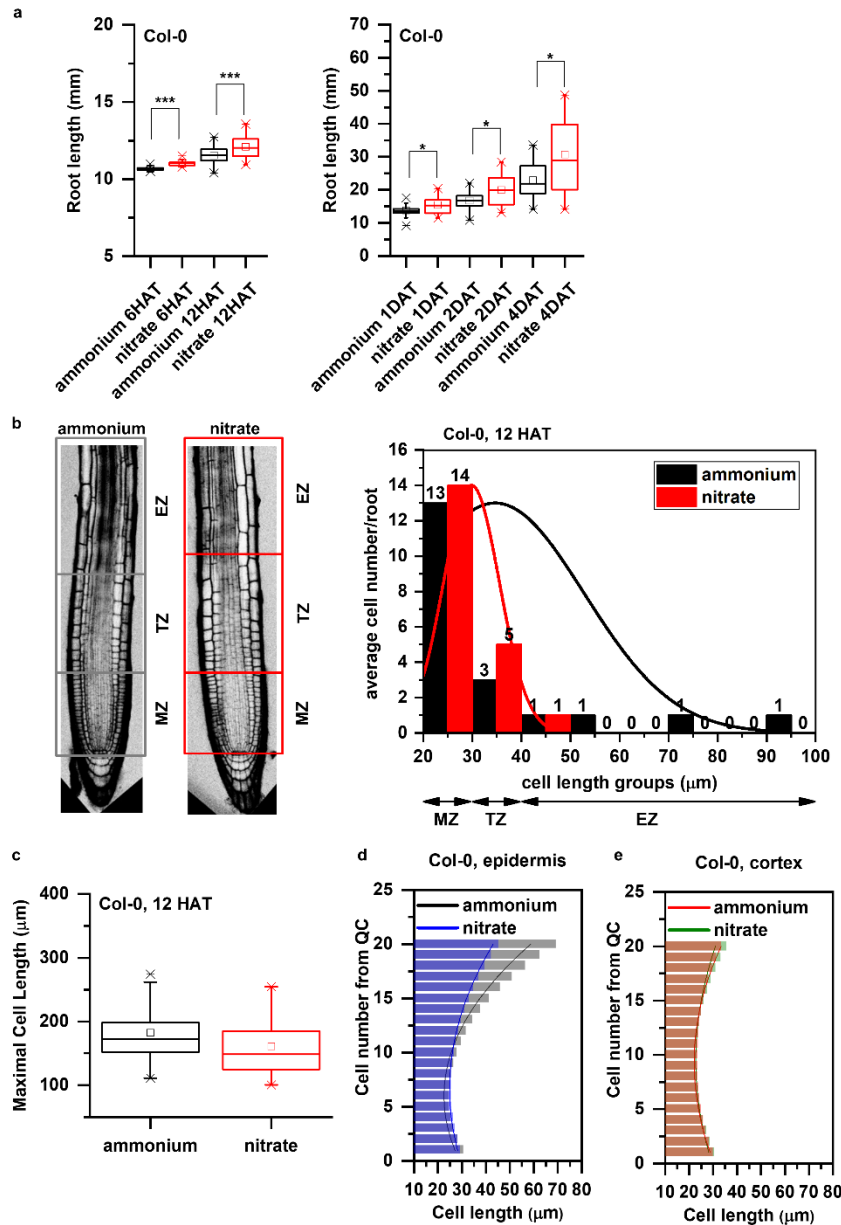


733 per genotype per treatment. The statistical significance was evaluated with ANOVA at  $p < 0.05$ .  
 734 **b - e.** Optical, longitudinal sections of 5 DAG old roots expressing *PIN2S439D-GFP* (**b and**  
 735 **c**) and *PIN2S439A-GFP* (**d and e**) 12 HAT to ammonium (**b and d**) or nitrate (**c and d**)  
 736 supplemented media. The first 20-20 epidermal and cortex cells (from quiescent center (QC))  
 737 are highlighted in grey and in red on ammonium (**b and d**) and in blue and green on nitrate (**c**  
 738 **and e**), respectively. Scale bar = 30  $\mu\text{m}$ . Column bars denote the geometric mean of cell length  
 739 at the respective positions. Lines represent a polynomial regression fit, with calculated slopes  
 740 between cells 10 and 20 of ammonium-PIN2S439D-epidermis:  $1.38867 + 0.03079x$ , ammonium-  
 741 PIN2S439D-cortex:  $0.05689 + 0.00497x$ , nitrate-PIN2S439D-epidermis:  $1.92749 + 0.0727x$ ,  
 742 nitrate-PIN2S439D-cortex:  $0.66477 + 0.03592x$ , ammonium-PIN2S439A-epidermis:  
 743  $0.7164 \pm 0.00565$ , ammonium-PIN2S439A-cortex:  $1.09064 \pm 0.05609$ , nitrate-PIN2S439A-  
 744 epidermis:  $0.53796 \pm 0.0249$ , nitrate-PIN2S439A-cortex:  $1.61118 \pm 0.09541$ . Data are derived  
 745 from 3 independent experiments; at least 5 roots were analyzed in each case.



746

747 **Figure 8. Dynamic computer model of root growth predicts nitrogen source dependent**  
748 **effect on cell growth dynamics, auxin distribution and root zonation. a.** Schematics of the  
749 root model with epidermis (ep) and cortex (co) tissues. Meristematic and elongating cells are  
750 shown with blue and yellow walls, respectively. Auxin levels are represented by green circle  
751 size and red bars reflect the PIN2 amounts. Auxin is supplied from Lateral Root Cap (LRC)  
752 and QC (Model B) **b.** Steady state snapshots from model simulation with ammonium (left  
753 panel) and with nitrate (right panel). Note out-of-sync growth patterns (dashed white line) in  
754 ammonium. **c and d.** Model simulation representing the effect of the transition from  
755 ammonium to nitrate (denoted by a red dashed line) on the relative level of auxin (C) and  
756 meristem size measured as distance from QC (D). **e.** Model predictions display the fraction of  
757 total cell division events per cell in the meristem along in the two N source. Note cell division  
758 is out-of-sync in ammonium, producing altered growth of the root. **f.** Experimentally derived  
759 relative auxin level threshold triggering cell elongation depends on the actual N content of the  
760 root.

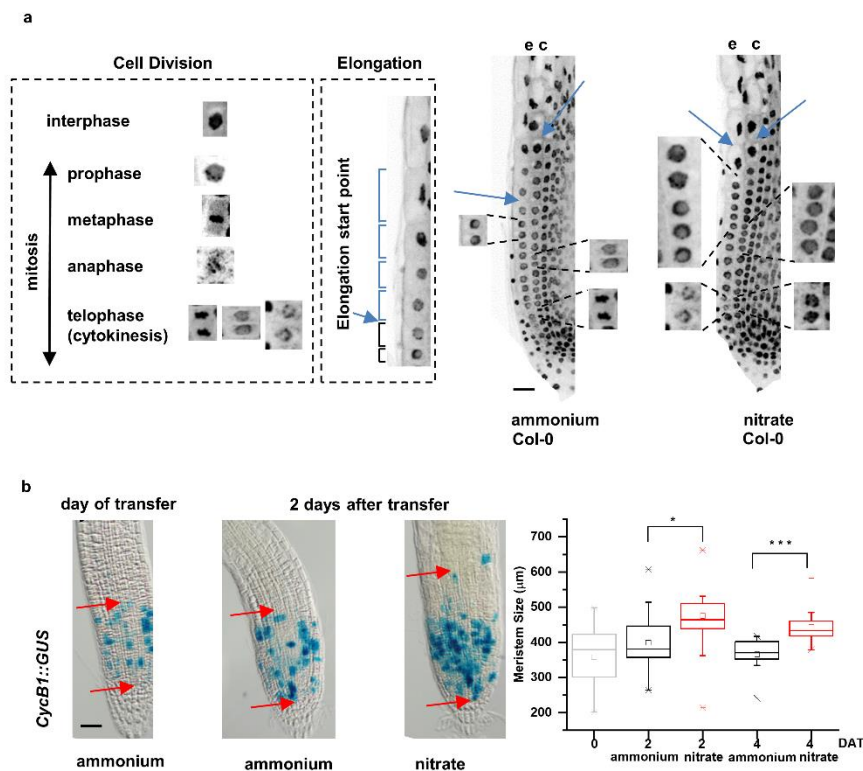


761

762 **Supplementary Figure 1 related to Figure 1. Additional data supporting the distinct**  
 763 **growth kinetics of Col-0 roots transferred to ammonium or nitrate supplemented media.**

764 **a.** Primary root length (mm) of Col-0 seedlings 6 and 12 HAT and 1, 2, 4 days after transfer  
 765 (DAT) to ammonium (black) or nitrate (red) supplemented medium. At least 34 roots were  
 766 measured per time point per treatment. The statistical significance was evaluated with ANOVA  
 767 at  $p < 0.05$ . **b.** On the left, schematic representation of distinct root zones: Meristematic Zone  
 768 (MZ), Transition Zone (TZ, which is interpolated between the apical meristem and the  
 769 subapical elongation zone) and Elongation Zone (EZ). Boxes highlight the borders of the  
 770 specified root zones (grey box for ammonium and red for nitrate). On the right, Col-0 epidermal  
 771 cells length was measured along the root tip (from QC), grouped based on their cell length (x

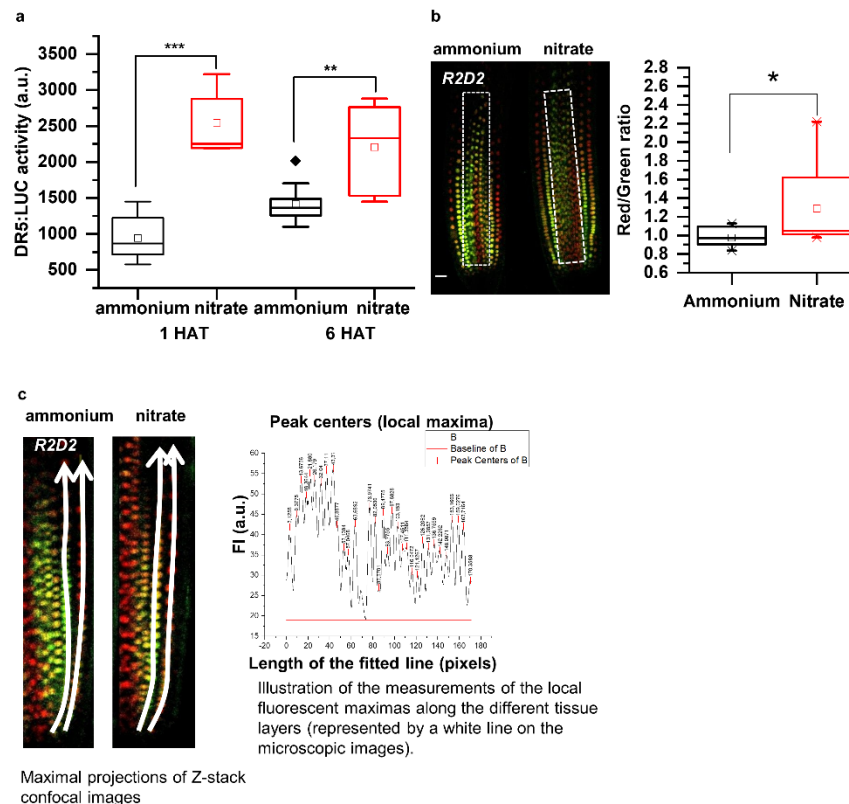
772 axis) and were plotted against the average cell number per group per root (y axis) in both  
 773 conditions (ammonium, black and nitrate, red). Note the higher cell number in case of nitrate  
 774 (red) in the group (30-40  $\mu\text{m}$ , representing TZ). Data are derived from 3 independent  
 775 experiments, total number of analyzed roots are n=18 in each case. **c.** Maximal cell length  
 776 (measured at the end of the elongation zone) of Col-0 roots 12 HAT either to ammonium  
 777 (black) or nitrate (red). 13 roots per treatment, 3 cells per root were analyzed. **d and e.**  
 778 Comparison of cell length measurements along epidermis (**d**) and cortex (**e**) upon ammonium  
 779 (black and red) and nitrate (blue and green) treatments. Column bars denote the geometric  
 780 mean of cell length at the respective positions. Lines represent a polynomial regression fit. Data  
 781 are derived from 3 independent experiments, total number of analyzed roots are n=18 in each  
 782 case.



783

784 **Supplementary Figure 2 related to Figure 1. Additional data supporting the distinct**  
 785 **division patterns in Col-0 roots on media supplemented with different nitrogen source. a.**  
 786 On the left, schematic representation of the different cell division phases of DAPI stained Col-0  
 787 roots and an illustration of how the onset of cell elongation was marked. On the right, DAPI  
 788 stained confocal microscopic images of Col-0 roots 12 HAT to ammonium or nitrate containing  
 789 medium. Mitotic events are displayed along epidermis (e) and cortex (c). Blue arrows point to  
 790 the first elongating cells. Scale bar = 50  $\mu\text{m}$ . **b.** Bright field microscopic images of *GUS*

791 expressing roots driven by *CycBI* promoter. Blue spots mark *CycBI* promoter activity. Red  
 792 arrows point to the beginning and to the end of GUS expressing area (meristem size). Scale bar  
 793 = 100 $\mu$ m. Box plot chart represents the meristem size ( $\mu$ m) of *CycBI::GUS* expressing roots  
 794 on the day of transfer (0) and 2 and 4 DAT to ammonium or nitrate. Differences of the means  
 795 were calculated with a t-test (p value  $* < 0.05$ ,  $*** < 0.001$ ). At least 14 roots were analyzed per  
 796 time point per treatment.

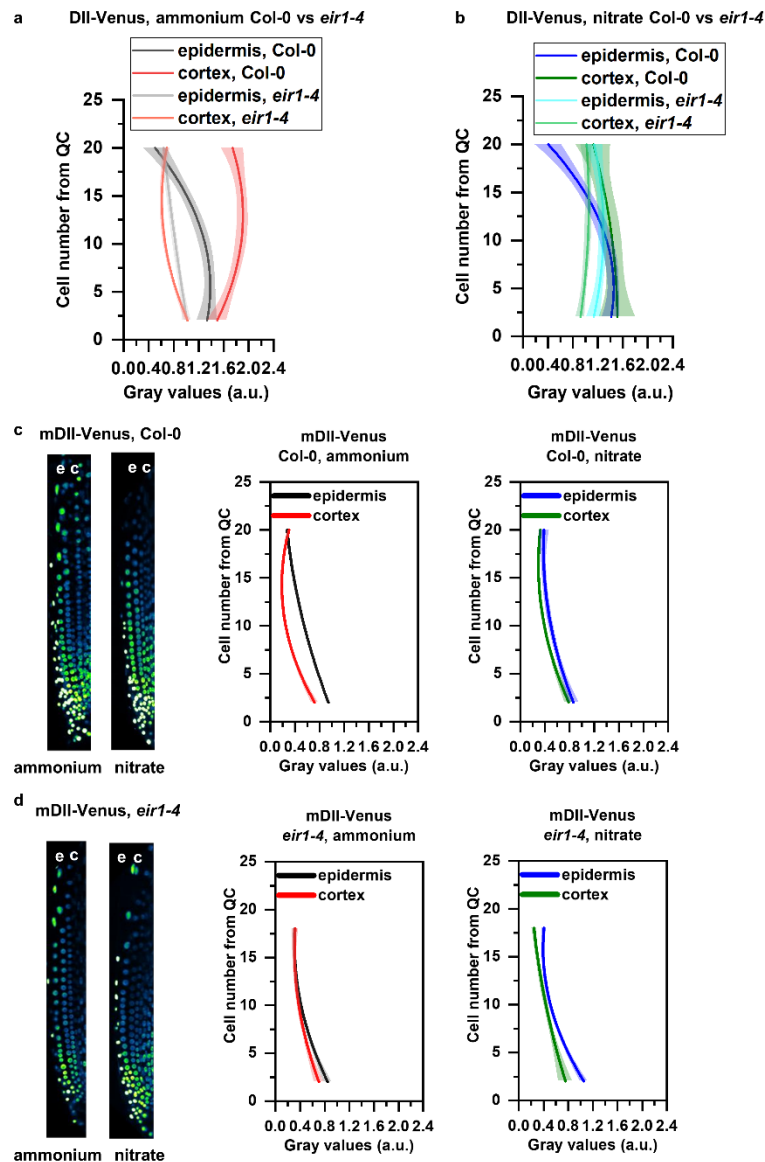


797

798 **Supplementary Figure 3 related to Figure 2. Supporting data for auxin activity and**  
 799 **distribution in roots transferred to different nitrogen sources.**

800 **a.** *DR5* activity in *Arabidopsis* roots. Box plots represents luciferase activities in *DR5::LUC*  
 801 expressing roots 1 and 6 HAT. 40 roots were collected per treatment per time points.  
 802 Experiment was repeated 3 times. Statistical differences were calculated with a t-test (p values  
 803  $** < 0.01$ ,  $*** < 0.001$ ) **b.** Expression profile of the auxin-input reporter *R2D2* in the stele  
 804 (labeled with “white box”) of roots 12 HAT to ammonium or nitrate containing media. Box  
 805 plots represent the quantification of the red (auxin-independent) vs green (auxin dependent)  
 806 fluorescent signal ratio in the stele. At least 13 roots were analyzed and statistical difference  
 807 was calculated with a t-test (p value  $< 0.05$ ). **c.** Illustrations for *R2D2* quantification along

808 epidermal and cortical cell files. For details see the “Quantification of R2D2, DII-VENUS and  
 809 mDII-VENUS fluorescence signal” in the “Methods” section.



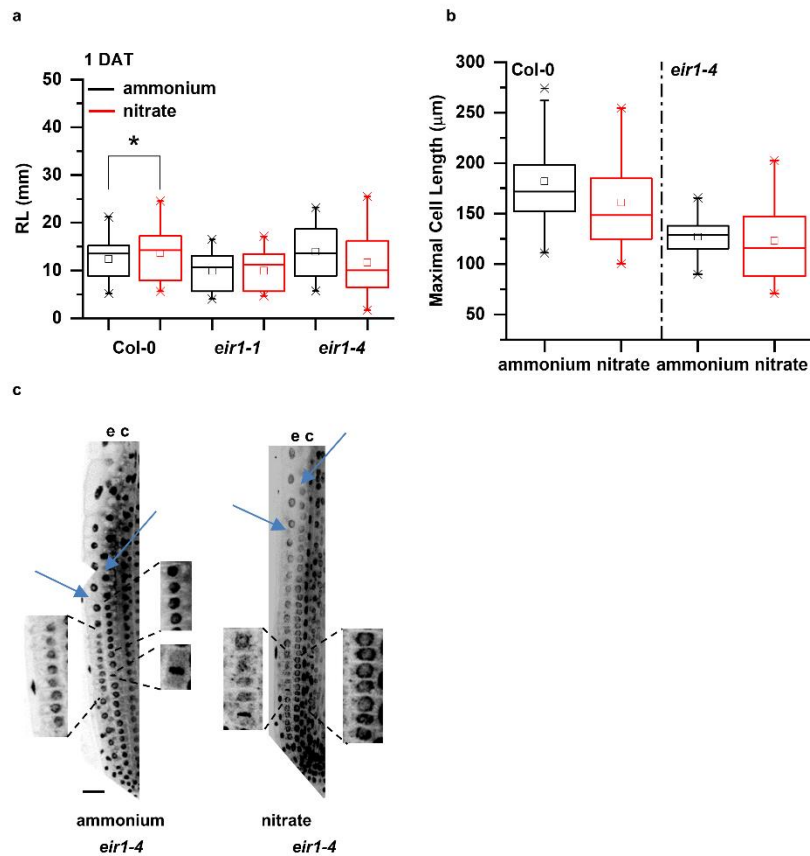
810

811 **Supplementary Figure 4 related to Figure 3. Additional data for demonstrating the**  
 812 **distinct patterns of auxin distribution in Col-0 and *eir1-4* roots**

813 **a and b.** Comparison of DII-Venus fluorescent signal in Col-0 and *eir1-4* lines on ammonium  
 814 (a) and on nitrate (b) transferred roots. Graphs denote normalized relative auxin levels at the  
 815 respective positions. Lines represent polynomial regression fit with 95% confidence band. Data  
 816 are derived from measurements of n=8 (ammonium) and n=10 (nitrate) roots of Col-0 and n=10  
 817 roots of *eir1-4* per condition. **c and d.** Maximum intensity Z-stack projection images of 5 DAG  
 818 old Col-0 (c) and *eir1-4* mutant (d) roots expressing the non-auxin degradable mDII-Venus  
 819 reporter grown on ammonium and nitrate supplemented media 12 HAT. “e” and “c” marks



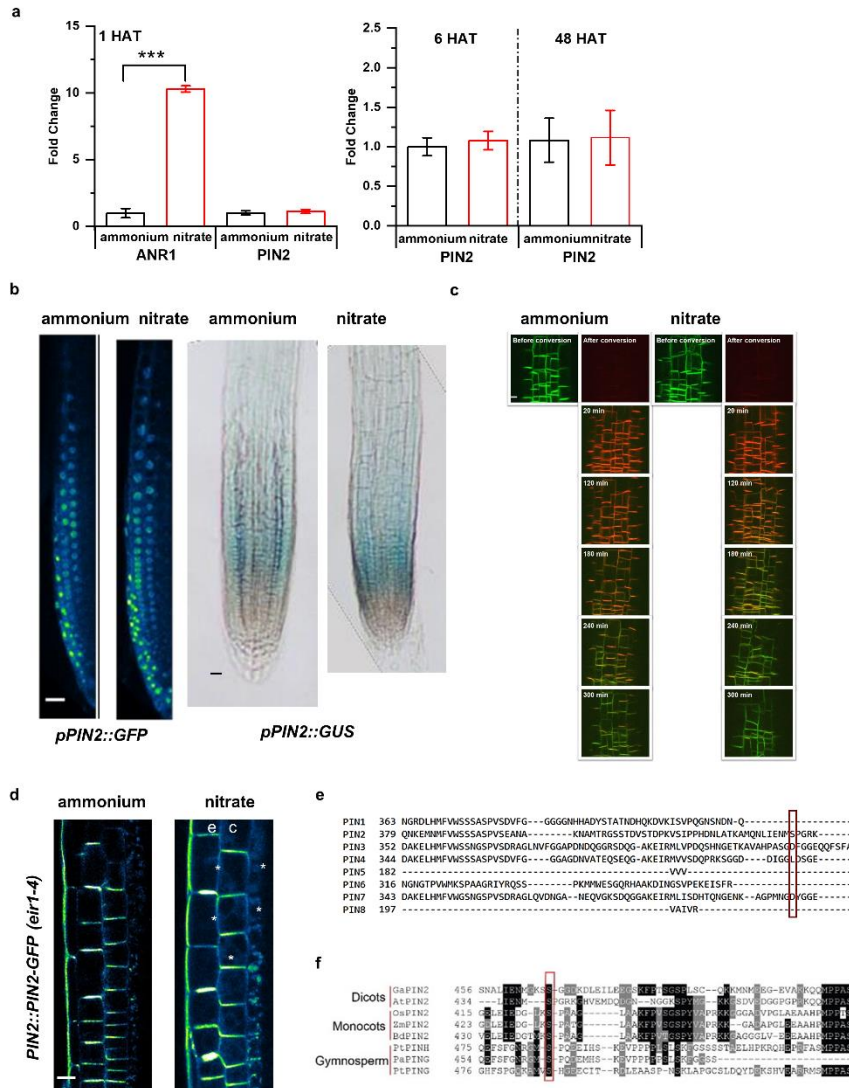
820 epidermis and cortex, respectively. Scale bar = 50  $\mu$ m. Graphs denote grey values (arbitrary  
821 units - a.u.) at the respective positions. Lines represent polynomial regression fit with 95%  
822 confidence band. Data are derived from measurements of at least 5 roots per genotype per  
823 treatment.



824

825 **Supplementary Figure 5 related to Figure 4. Additional data for demonstrating root**  
826 **growth phenotypes and cell divisions in *pin2* mutants**

827 **a.** Comparison of root length of *pin2* mutants (*eir1-1* and *eir1-4*) to Col-0 on ammonium  
828 (black) and nitrate (red) amended media, 1 DAT. At least 11 roots were analyzed per genotype  
829 per treatment and statistical difference was calculated with a t-test (p value <0.001) **b.** Box  
830 plots of the maximal cell length of Col-0 and *eir1-4* mutant roots 12 HAT to ammonium (black)  
831 or nitrate (red). 3-3 cells in at least 13 roots were analyzed per genotype per treatment. **c.** DAPI  
832 stained confocal microscopic images of *eir1-4* roots 12 HAT to ammonium or nitrate  
833 containing medium. Mitotic events are highlighted along epidermis (e) and cortex (c). Blue  
834 arrows point to the first elongating cells. Scale bar = 50  $\mu$ m.

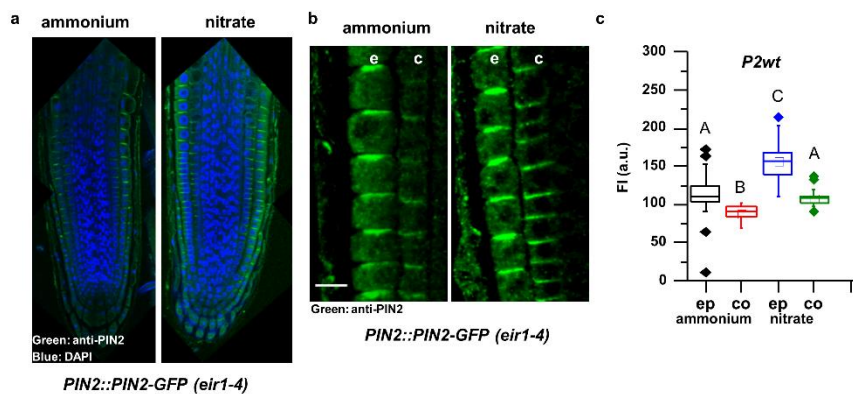


835

836 **Supplementary Figure 6 related to Figure 5. Additional data supporting distinct effects**  
 837 **of nitrogen sources on PIN2**

838 **a.** RT-qPCR analysis of *PIN2* expression normalized to *UBQ10* (*AT4G05320*) levels in Col-0  
 839 roots 1, 6 and 48 HAT to ammonium or nitrate. As a positive control, expression of *ANR1*  
 840 (nitrate responsive MADS-box transcription factor) was quantified. All RT-qPCR reactions  
 841 were carried out with biological and technical triplicates. Statistical difference was calculated  
 842 with a t-test (p value \*\*\*<0.001). **b.** *PIN2* promoter activity was monitored in *pPIN2::nlsGFP*  
 843 and *pPIN2::GUS* expressing roots 12 HAT to ammonium or nitrate. Scale bars = 50  $\mu$ m. **c.**  
 844 Confocal microscopic images of *PIN2::PIN2-DENDRA* fluorescence in the same area of the  
 845 root transition zones 12 HAT to ammonium or nitrate before and after photoconversion (0, 20,  
 846 120, 180, 240, 300 min). Scale bar = 20  $\mu$ m. **d.** Multiphoton microscopic image showing  
 847 polarity changes of *PIN2* expression upon nitrate treatment. “e” and “c” denote epidermis and

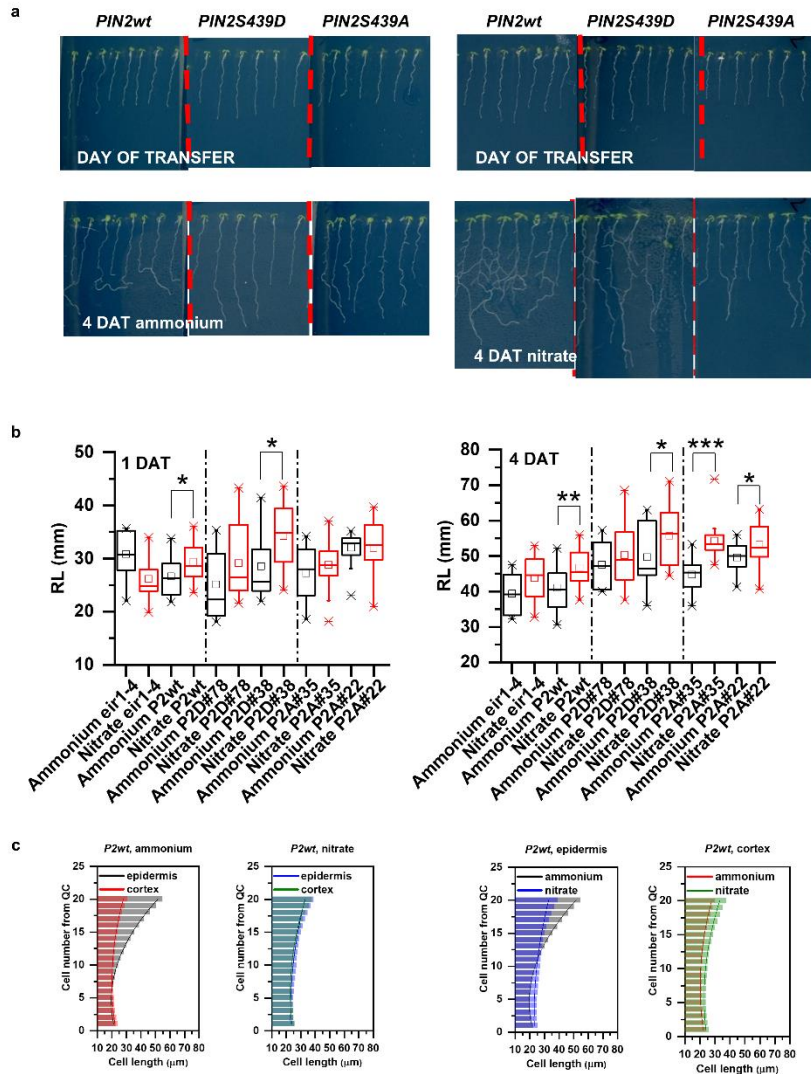
848 cortex respectively. White arrows mark lateralization of the PIN2-GFP signal in cortex cells  
849 (c). **e.** Protein sequence alignment of members of the *Arabidopsis* PIN protein family. Ser439  
850 of PIN2 and the corresponding residues of other PIN family members are marked by a red box.  
851 **f.** PIN2 protein sequence alignment shows evolutionary conservation of Ser439 in  
852 representative members of Gymnosperms, Monocots and Dicots. From Gymnosperms *Picea*  
853 *abies* (Pa) and *Pinus taeda* (Pt) PIN2 proteins (PtPING, PtPINH, PaPING), from Monocots  
854 *Zea mays* (Zm), *Brachypodium distachyon* (Bd) and *Oryza sativa* (Os) PIN2 proteins  
855 (ZmPIN2, BdPIN2, OsPIN2) and from Dicots *Gossypium arboreun* (Ga) and *Arabidopsis*  
856 *thaliana* (At) PIN2 proteins (GaPIN2, AtPIN2) were used. Protein alignments were created  
857 with the MEGAX software<sup>66</sup>.



858

### 859 **Supplementary Figure 7 related to Figure 5a. PIN2 immunostaining in *PIN2-GFP*** 860 **expressing roots**

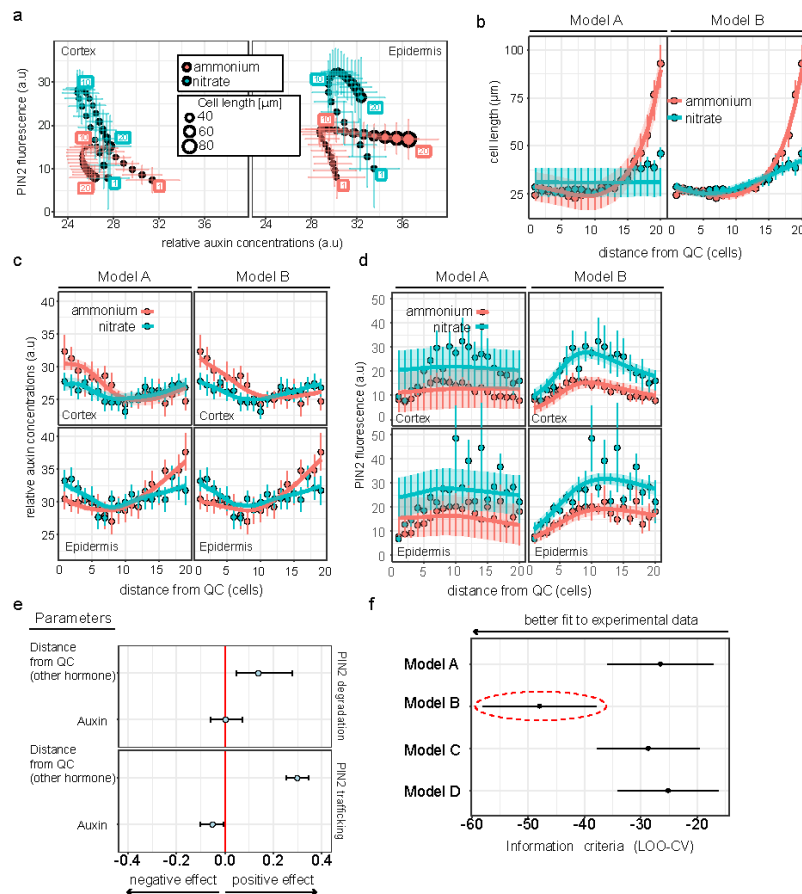
861 **a.** Confocal microscopic images show anti-PIN2 immunostained *PIN2-GFP* expressing root  
862 tips 12 HAT to ammonium or nitrate. Green and blue signal represents PIN2 and nuclear  
863 staining with DAPI, respectively. **b.** Higher magnification of anti-PIN2 immunostained *PIN2-*  
864 *GFP* expressing root in the transition zone. “e” and “c” denote epidermis and cortex,  
865 respectively. Scale bar = 25  $\mu$ m. **c.** Quantification of PIN2 fluorescent signal in the  
866 immunostained, ammonium or nitrate treated roots in epidermal (ep) and cortical (co) cell files.  
867 Statistical difference was evaluated with ANOVA at  $p < 0.05$ . 10 roots were analyzed per  
868 treatment.



869

870 **Supplementary Figure 8 related to Figure 7. Additional data supporting impact of**  
 871 ***PIN2S439* phospho-variants on root growth adaptation to source of nitrogen**

872 **a, b.** Seedlings expressing *PIN2::PIN2-GFP* (*P2wt*), *PIN2::PIN2S439D-GFP* (*P2D*) and  
 873 *PIN2::PIN2S439A-GFP* (*P2A*) in *eir1-4* background. Representative images of seedlings at the  
 874 day of transfer and 4 DAT to ammonium or nitrate supplemented plates are shown (a).  
 875 Quantification of root length (mm) in *eir1-4*, *PIN2wt* (*eir1-4*) and two independent *P2D* (*eir1-*  
 876 *4*) (#78 and #38) and *P2A* (*eir1-4*) (#35 and #22) lines 1 and 4 DAT to ammonium or nitrate  
 877 containing media. At least 7 roots per genotype per treatment were analyzed. Statistical  
 878 difference was evaluated with a t-test (p values \* $<0.05$ , \*\* $<0.01$  and \*\*\* $<0.001$ ). **c.**  
 879 Comparison of cell length changes in epidermal and cortical cell files of *PIN2::PIN2-GFP*  
 880 (*P2wt*) expressing roots transferred to ammonium or nitrate. Column bars denote the geometric  
 881 mean of cell length at the respective positions. Lines represent a polynomial regression fit. Data  
 882 are derived from measurements of 20 roots per genotype per treatment.



883

884 **Supplementary Figure 9. Model robustness and fitting to experimental measurements. a.**

885 The experimentally-driven PIN2 levels in the function of relative auxin levels for cortex (left

886 panel) and epidermis (right panel), respectively. Relative auxin levels were calculated as

887 follows:  $\log(G/(G+R)) / -0.025$ , where G and R represent DII-Venus (green) and mDII-Tomato

888 (red) fluorescent signals, respectively. Cell length is denoted by dot size, and the distance of

889 the cell from the QC is labelled with consecutive numbers. Vertical and horizontal lines

890 represent the standard error of measurements. **b-d.** Validations in two regimes demonstrate that

891 Model B faithfully recapitulates all experimental measurements. In these plots model

892 predictions (thick lines and shaded areas for the posterior average and 95% confidence

893 intervals, respectively) are plotted against experimental data (dots and vertical bars for data

894 mean and standard deviations, respectively). **e.** Parameter estimations for Model B suggest

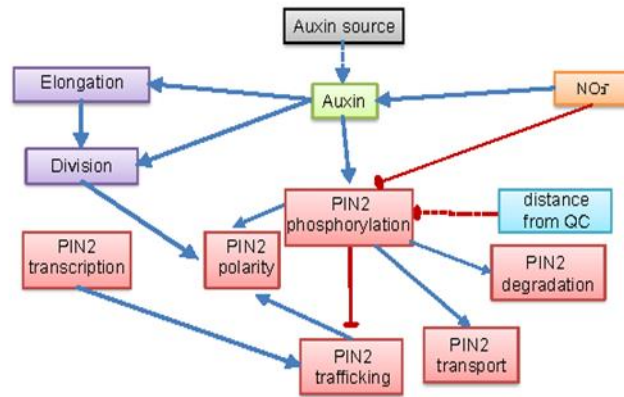
895 antithetic cumulative effects of auxin level and distance from QC on PIN2 dynamics. **f.**

896 Predictive power of four models for auxin input scenario (A-D). The expected log probability

897 density is used as information criterion. Lower information criterion indicates better posterior

898 predictive performance, and therefore a better fit to the experiments (dashed red ellipse).





899

900 **Supplementary Figure 10. Model diagram.** The graphical chart representing the  
901 relationships between molecular and structural root processes assumed in the computational  
902 model. Solid lines indicated correlation whose effects have been demonstrated (either in our  
903 experiments or previous studies). Dashed lines are for relationships that have been integrated  
904 in the current model. The two main regulators considered in the model are auxin and nitrate  
905 levels, which exert an antithetic effect on PIN2 dynamics through phosphorylation.

906 **Link to Supplementary videos:**

907 [https://drive.google.com/drive/folders/1AAqNEYuGH2jSOvb\\_ffvLYYxyF\\_eLJSK?usp=sh](https://drive.google.com/drive/folders/1AAqNEYuGH2jSOvb_ffvLYYxyF_eLJSK?usp=sharing)  
908 [aring](https://drive.google.com/drive/folders/1AAqNEYuGH2jSOvb_ffvLYYxyF_eLJSK?usp=sharing)

909 **Supplementary Video 1 related to Figure 1a.**

910 Time lapse of 5 days old *Arabidopsis* roots expressing the PM marker (*WAVE131Y*) transferred  
911 to either on ammonium or nitrate supplemented media and imaged with a vertically oriented  
912 LSM700 microscope. Observation of roots initiated 20 minutes after transfer and images  
913 recorded every 20 minutes (9 stacks/root/ recording).

914 **Supplementary Video 2 related to Figure 1b.**

915 Time lapse of the transition zone of 5-day-old *Arabidopsis* roots expressing the PM marker  
916 (*WAVE131Y*) transferred to either on ammonium or nitrate amended media and imaged with a  
917 vertically oriented LSM700 microscope. Observation of roots initiated 20 minutes after transfer  
918 and images recorded every 20 minutes (9 stacks/root/ recording).

919 **Supplementary Video 3 related to Figure 5.**



920 Z-stacks of 2-2 cells in the transition zone of 5-day-old *Arabidopsis* roots expressing  
921 *PIN2::PIN2-GFP* 12 HAT to either to ammonium or nitrate amended media and imaged with  
922 an Airyscan LSM800 microscope.

923 **Supplementary Video 4 related to Figure 7.**

924 Time lapse of *Arabidopsis* seedlings expressing *PIN2::PIN2-GFP* (*PIN2wt*),  
925 *PIN2::PIN2S439D-GFP* (*PIN2S439D*) and *PIN2::PIN2S439A-GFP* (*PIN2S439A*). Seedlings  
926 were grown on ammonium plates for 7 days and were transferred to ammonium containing  
927 agar plates. Plates were scanned on a daily basis with an Epson Perfection V700 flatbed  
928 scanner. Images were concatenated with Fiji.

929 **Supplementary Video 5 related to Figure 7.**

930 Time lapse of *Arabidopsis* seedlings expressing wild type *PIN2::PIN2-GFP* (*PIN2wt*),  
931 *PIN2::PIN2S439D-GFP* (*PIN2S439D*) and *PIN2::PIN2S439A-GFP* (*PIN2S439A*). Seedlings  
932 were grown on ammonium plates for 7 days and were transferred to nitrate containing agar  
933 plates. Plates were scanned on a daily basis with an Epson Perfection V700 flatbed scanner.  
934 Images were concatenated with Fiji.

935 **Supplementary Video 6 related to Figure 8.**

936 A simulation of static example model shows intercellular auxin transport via PIN2 auxin  
937 carrier.

938 **Supplementary Video 7 related to Figure 8.**

939 Simulation of asynchronous growth of epidermis-cortex tissues in ammonium condition.  
940 Related to Fig. 8b.

941 **Supplementary Video 8 related to Figure 8.**

942 Simulation of asynchronous growth of epidermis-cortex tissues in nitrate condition. Related to  
943 Fig. 8b.

A. ammonium						nitrate							
1. Position = 1, Treatment = ammonium:						Position = 1, Treatment = nitrate:							
Tissue	emmean	SE	df	asympt.LCL	asympt.UCL	.group	Tissue	emmean	SE	df	asympt.LCL	asympt.UCL	.group
cortex	0.0362	0.002373	Inf	0.03085	0.0415	a	cortex	0.0342	0.002242	Inf	0.02914	0.0392	a
epidermis	0.0416	0.002734	Inf	0.03554	0.0478	a	epidermis	0.0345	0.002265	Inf	0.02944	0.0396	a
2. Position = 2, Treatment = ammonium:						Position = 2, Treatment = nitrate:							
Tissue	emmean	SE	df	asympt.LCL	asympt.UCL	.group	Tissue	emmean	SE	df	asympt.LCL	asympt.UCL	.group
cortex	0.0388	0.002548	Inf	0.03312	0.0445	a	cortex	0.0377	0.002475	Inf	0.03211	0.0432	a
epidermis	0.0369	0.002419	Inf	0.03145	0.0423	a	epidermis	0.0371	0.002437	Inf	0.03168	0.0426	a
3. Position = 3, Treatment = ammonium:						Position = 3, Treatment = nitrate:							
Tissue	emmean	SE	df	asympt.LCL	asympt.UCL	.group	Tissue	emmean	SE	df	asympt.LCL	asympt.UCL	.group
cortex	0.0354	0.002326	Inf	0.03023	0.0406	a	cortex	0.0376	0.002470	Inf	0.03211	0.0432	a
epidermis	0.0378	0.002480	Inf	0.03224	0.0433	a	epidermis	0.0367	0.002408	Inf	0.03131	0.0421	a
4. Position = 4, Treatment = ammonium:						Position = 4, Treatment = nitrate:							
Tissue	emmean	SE	df	asympt.LCL	asympt.UCL	.group	Tissue	emmean	SE	df	asympt.LCL	asympt.UCL	.group
cortex	0.0390	0.002557	Inf	0.03324	0.0447	a	cortex	0.0381	0.002498	Inf	0.03248	0.0437	a
epidermis	0.0369	0.002423	Inf	0.03150	0.0423	a	epidermis	0.0383	0.002511	Inf	0.03264	0.0439	a
5. Position = 5, Treatment = ammonium:						Position = 5, Treatment = nitrate:							
Tissue	emmean	SE	df	asympt.LCL	asympt.UCL	.group	Tissue	emmean	SE	df	asympt.LCL	asympt.UCL	.group
cortex	0.0387	0.002539	Inf	0.03301	0.0444	a	cortex	0.0425	0.002790	Inf	0.03627	0.0487	a
epidermis	0.0366	0.002403	Inf	0.03124	0.0420	a	epidermis	0.0391	0.002567	Inf	0.03337	0.0448	a
6. Position = 6, Treatment = ammonium:						Position = 6, Treatment = nitrate:							
Tissue	emmean	SE	df	asympt.LCL	asympt.UCL	.group	Tissue	emmean	SE	df	asympt.LCL	asympt.UCL	.group
cortex	0.0398	0.002610	Inf	0.03393	0.0456	a	cortex	0.0414	0.002720	Inf	0.03536	0.0475	a
epidermis	0.0415	0.002725	Inf	0.03542	0.0476	a	epidermis	0.0366	0.002401	Inf	0.03122	0.0420	a
7. Position = 7, Treatment = ammonium:						Position = 7, Treatment = nitrate:							
Tissue	emmean	SE	df	asympt.LCL	asympt.UCL	.group	Tissue	emmean	SE	df	asympt.LCL	asympt.UCL	.group
cortex	0.0444	0.002916	Inf	0.03791	0.0509	a	cortex	0.0406	0.002666	Inf	0.03466	0.0466	a
epidermis	0.0434	0.002850	Inf	0.03705	0.0498	a	epidermis	0.0364	0.002392	Inf	0.03110	0.0418	a
8. Position = 8, Treatment = ammonium:						Position = 8, Treatment = nitrate:							
Tissue	emmean	SE	df	asympt.LCL	asympt.UCL	.group	Tissue	emmean	SE	df	asympt.LCL	asympt.UCL	.group
cortex	0.0426	0.002798	Inf	0.03637	0.0489	a	cortex	0.0397	0.002606	Inf	0.03387	0.0455	a
epidermis	0.0408	0.002676	Inf	0.03479	0.0468	a	epidermis	0.0369	0.002424	Inf	0.03152	0.0424	a
9. Position = 9, Treatment = ammonium:						Position = 9, Treatment = nitrate:							
Tissue	emmean	SE	df	asympt.LCL	asympt.UCL	.group	Tissue	emmean	SE	df	asympt.LCL	asympt.UCL	.group
cortex	0.0426	0.002795	Inf	0.03634	0.0488	a	cortex	0.0423	0.002776	Inf	0.03609	0.0485	a
epidermis	0.0392	0.0022570	Inf	0.03342	0.0449	a	epidermis	0.0392	0.002576	Inf	0.03349	0.0450	a
10. Position = 10, Treatment = ammonium:						Position = 10, Treatment = nitrate:							
Tissue	emmean	SE	df	asympt.LCL	asympt.UCL	.group	Tissue	emmean	SE	df	asympt.LCL	asympt.UCL	.group
cortex	0.0448	0.002942	Inf	0.03824	0.0514	a	cortex	0.0431	0.002831	Inf	0.03680	0.0495	a
epidermis	0.0380	0.002497	Inf	0.03246	0.0436	a	epidermis	0.0394	0.002583	Inf	0.03359	0.0451	a
11. Position = 11, Treatment = ammonium:						Position = 11, Treatment = nitrate:							
Tissue	emmean	SE	df	asympt.LCL	asympt.UCL	.group	Tissue	emmean	SE	df	asympt.LCL	asympt.UCL	.group
cortex	0.0472	0.003096	Inf	0.04025	0.0541	a	cortex	0.0408	0.002677	Inf	0.03480	0.0468	a
epidermis	0.0341	0.002236	Inf	0.02907	0.0391	b	epidermis	0.0370	0.002432	Inf	0.03161	0.0425	a
12. Position = 12, Treatment = ammonium:						Position = 12, Treatment = nitrate:							
Tissue	emmean	SE	df	asympt.LCL	asympt.UCL	.group	Tissue	emmean	SE	df	asympt.LCL	asympt.UCL	.group
cortex	0.0448	0.002942	Inf	0.03825	0.0514	a	cortex	0.0424	0.002783	Inf	0.03618	0.0486	a
epidermis	0.0349	0.002288	Inf	0.02974	0.0400	b	epidermis	0.0354	0.002326	Inf	0.03024	0.0406	a
13. Position = 13, Treatment = ammonium:						Position = 13, Treatment = nitrate:							
Tissue	emmean	SE	df	asympt.LCL	asympt.UCL	.group	Tissue	emmean	SE	df	asympt.LCL	asympt.UCL	.group
cortex	0.0426	0.002798	Inf	0.03638	0.0489	a	cortex	0.0410	0.002688	Inf	0.03494	0.0470	a
epidermis	0.0352	0.002309	Inf	0.03002	0.0404	b	epidermis	0.0332	0.002182	Inf	0.02836	0.0381	b
14. Position = 14, Treatment = ammonium:						Position = 14, Treatment = nitrate:							
Tissue	emmean	SE	df	asympt.LCL	asympt.UCL	.group	Tissue	emmean	SE	df	asympt.LCL	asympt.UCL	.group
cortex	0.0437	0.002867	Inf	0.03727	0.0501	a	cortex	0.0420	0.002756	Inf	0.03582	0.0481	a
epidermis	0.0310	0.002035	Inf	0.02646	0.0356	b	epidermis	0.0313	0.002056	Inf	0.02673	0.0359	b
15. Position = 15, Treatment = ammonium:						Position = 15, Treatment = nitrate:							
Tissue	emmean	SE	df	asympt.LCL	asympt.UCL	.group	Tissue	emmean	SE	df	asympt.LCL	asympt.UCL	.group
cortex	0.0403	0.002647	Inf	0.03441	0.0462	a	cortex	0.0421	0.002761	Inf	0.03590	0.0482	a
epidermis	0.0277	0.001820	Inf	0.02366	0.0318	b	epidermis	0.0302	0.001982	Inf	0.02576	0.0346	b
16. Position = 16, Treatment = ammonium:						Position = 16, Treatment = nitrate:							
Tissue	emmean	SE	df	asympt.LCL	asympt.UCL	.group	Tissue	emmean	SE	df	asympt.LCL	asympt.UCL	.group
cortex	0.0370	0.002427	Inf	0.03156	0.0424	a	cortex	0.0394	0.002588	Inf	0.03365	0.0452	a
epidermis	0.0233	0.001530	Inf	0.01989	0.0267	b	epidermis	0.0252	0.001652	Inf	0.02148	0.0289	b
17. Position = 17, Treatment = ammonium:						Position = 17, Treatment = nitrate:							
Tissue	emmean	SE	df	asympt.LCL	asympt.UCL	.group	Tissue	emmean	SE	df	asympt.LCL	asympt.UCL	.group
cortex	0.0330	0.002168	Inf	0.02818	0.0379	a	cortex	0.0373	0.002448	Inf	0.03182	0.0428	a
epidermis	0.0212	0.001390	Inf	0.01806	0.0243	b	epidermis	0.0256	0.001731	Inf	0.02176	0.0295	b
18. Position = 18, Treatment = ammonium:						Position = 18, Treatment = nitrate:							
Tissue	emmean	SE	df	asympt.LCL	asympt.UCL	.group	Tissue	emmean	SE	df	asympt.LCL	asympt.UCL	.group
cortex	0.0310	0.002033	Inf	0.02643	0.0355	a	cortex	0.0332	0.002179	Inf	0.02832	0.0381	a
epidermis	0.0176	0.001157	Inf	0.01504	0.0202	b	epidermis	0.0241	0.001676	Inf	0.02032	0.0278	b
19. Position = 19, Treatment = ammonium:						Position = 19, Treatment = nitrate:							
Tissue	emmean	SE	df	asympt.LCL	asympt.UCL	.group	Tissue	emmean	SE	df	asympt.LCL	asympt.UCL	.group
cortex	0.0298	0.002075	Inf	0.02517	0.0345	a	cortex	0.0293	0.001921	Inf	0.02497	0.0336	a
epidermis	0.0127	0.000944	Inf	0.01057	0.0148	b	epidermis	0.0253	0.001954	Inf	0.02094	0.0297	a
20. Position = 20, Treatment = ammonium:						Position = 20, Treatment = nitrate:							
Tissue	emmean	SE	df	asympt.LCL	asympt.UCL	.group	Tissue	emmean	SE	df	asympt.LCL	asympt.UCL	.group
cortex	0.0278	0.002066	Inf	0.02314	0.0324	a	cortex	0.0254	0.001669	Inf	0.02170	0.0292	a
epidermis	0.0104	0.000870	Inf	0.00842	0.0123	b	epidermis	0.0218	0.001685	Inf	0.01805	0.0256	a

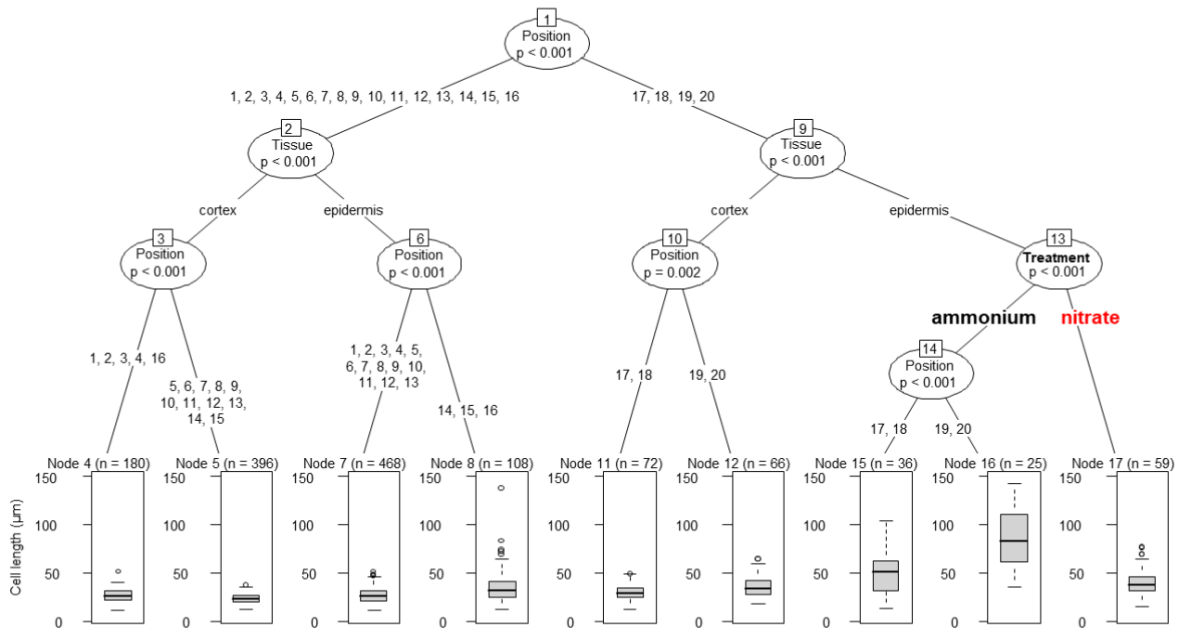
**B.**

**epidermis**

**cortex**

1. Position = 1, Tissue = epidermis:	Treatment emmean SE df asymp.LCL asymp.UCL .group ammonium 0.0416 0.002734 Inf 0.03554 0.0478 a nitrate 0.0345 0.002265 Inf 0.02944 0.0396 b	Position = 1, Tissue = cortex:	Treatment emmean SE df asymp.LCL asymp.UCL .group ammonium 0.0362 0.002373 Inf 0.03085 0.0415 a nitrate 0.0342 0.002242 Inf 0.02914 0.0392 a
2. Position = 2, Tissue = epidermis:	Treatment emmean SE df asymp.LCL asymp.UCL .group ammonium 0.0369 0.002419 Inf 0.03145 0.0423 a nitrate 0.0371 0.002437 Inf 0.03168 0.0426 a	Position = 2, Tissue = cortex:	Treatment emmean SE df asymp.LCL asymp.UCL .group ammonium 0.0388 0.002548 Inf 0.03312 0.0445 a nitrate 0.0377 0.002475 Inf 0.03217 0.0432 a
3. Position = 3, Tissue = epidermis:	Treatment emmean SE df asymp.LCL asymp.UCL .group ammonium 0.0378 0.002480 Inf 0.03224 0.0433 a nitrate 0.0367 0.002408 Inf 0.03131 0.0421 a	Position = 3, Tissue = cortex:	Treatment emmean SE df asymp.LCL asymp.UCL .group ammonium 0.0354 0.002326 Inf 0.03023 0.0406 a nitrate 0.0376 0.002470 Inf 0.03211 0.0432 a
4. Position = 4, Tissue = epidermis:	Treatment emmean SE df asymp.LCL asymp.UCL .group ammonium 0.0369 0.002423 Inf 0.03150 0.0423 a nitrate 0.0383 0.002511 Inf 0.03264 0.0439 a	Position = 4, Tissue = cortex:	Treatment emmean SE df asymp.LCL asymp.UCL .group ammonium 0.0390 0.002557 Inf 0.03324 0.0447 a nitrate 0.0381 0.002498 Inf 0.03248 0.0437 a
5. Position = 5, Tissue = epidermis:	Treatment emmean SE df asymp.LCL asymp.UCL .group ammonium 0.0366 0.002403 Inf 0.03124 0.0420 a nitrate 0.0391 0.002567 Inf 0.03337 0.0448 a	Position = 5, Tissue = cortex:	Treatment emmean SE df asymp.LCL asymp.UCL .group ammonium 0.0387 0.002539 Inf 0.03301 0.0444 a nitrate 0.0425 0.002790 Inf 0.03627 0.0487 a
6. Position = 6, Tissue = epidermis:	Treatment emmean SE df asymp.LCL asymp.UCL .group ammonium 0.0415 0.002725 Inf 0.03542 0.0476 a nitrate 0.0366 0.002401 Inf 0.03122 0.0420 a	Position = 6, Tissue = cortex:	Treatment emmean SE df asymp.LCL asymp.UCL .group ammonium 0.0398 0.002610 Inf 0.03393 0.0456 a nitrate 0.0414 0.002720 Inf 0.03536 0.0475 a
7. Position = 7, Tissue = epidermis:	Treatment emmean SE df asymp.LCL asymp.UCL .group ammonium 0.0434 0.002850 Inf 0.03705 0.0498 a nitrate 0.0364 0.002392 Inf 0.03110 0.0418 a	Position = 7, Tissue = cortex:	Treatment emmean SE df asymp.LCL asymp.UCL .group ammonium 0.0444 0.002916 Inf 0.03791 0.0509 a nitrate 0.0406 0.002666 Inf 0.03466 0.0466 a
8. Position = 8, Tissue = epidermis:	Treatment emmean SE df asymp.LCL asymp.UCL .group ammonium 0.0408 0.002676 Inf 0.03479 0.0468 a nitrate 0.0369 0.002424 Inf 0.03152 0.0424 a	Position = 8, Tissue = cortex:	Treatment emmean SE df asymp.LCL asymp.UCL .group ammonium 0.0426 0.002798 Inf 0.03637 0.0489 a nitrate 0.0397 0.002606 Inf 0.03387 0.0455 a
9. Position = 9, Tissue = epidermis:	Treatment emmean SE df asymp.LCL asymp.UCL .group ammonium 0.0392 0.002570 Inf 0.03342 0.0449 a nitrate 0.0392 0.002576 Inf 0.03349 0.0450 a	Position = 9, Tissue = cortex:	Treatment emmean SE df asymp.LCL asymp.UCL .group ammonium 0.0426 0.002795 Inf 0.03634 0.0488 a nitrate 0.0423 0.002776 Inf 0.03609 0.0485 a
10. Position = 10, Tissue = epidermis:	Treatment emmean SE df asymp.LCL asymp.UCL .group ammonium 0.0380 0.002497 Inf 0.03246 0.0436 a nitrate 0.0394 0.002583 Inf 0.03359 0.0451 a	Position = 10, Tissue = cortex:	Treatment emmean SE df asymp.LCL asymp.UCL .group ammonium 0.0448 0.002942 Inf 0.03824 0.0514 a nitrate 0.0431 0.002831 Inf 0.03680 0.0495 a
11. Position = 11, Tissue = epidermis:	Treatment emmean SE df asymp.LCL asymp.UCL .group ammonium 0.0341 0.002236 Inf 0.02907 0.0391 a nitrate 0.0370 0.002432 Inf 0.03161 0.0425 a	Position = 11, Tissue = cortex:	Treatment emmean SE df asymp.LCL asymp.UCL .group ammonium 0.0472 0.003096 Inf 0.04025 0.0541 a nitrate 0.0408 0.002677 Inf 0.03480 0.0468 a
12. Position = 12, Tissue = epidermis:	Treatment emmean SE df asymp.LCL asymp.UCL .group ammonium 0.0349 0.002288 Inf 0.02974 0.0400 a nitrate 0.0354 0.002326 Inf 0.03024 0.0406 a	Position = 12, Tissue = cortex:	Treatment emmean SE df asymp.LCL asymp.UCL .group ammonium 0.0448 0.002942 Inf 0.03825 0.0514 a nitrate 0.0424 0.002783 Inf 0.03618 0.0486 a
13. Position = 13, Tissue = epidermis:	Treatment emmean SE df asymp.LCL asymp.UCL .group ammonium 0.0352 0.002309 Inf 0.03002 0.0404 a nitrate 0.0332 0.002182 Inf 0.02836 0.0381 a	Position = 13, Tissue = cortex:	Treatment emmean SE df asymp.LCL asymp.UCL .group ammonium 0.0426 0.002798 Inf 0.03638 0.0489 a nitrate 0.0410 0.002688 Inf 0.03494 0.0470 a
14. Position = 14, Tissue = epidermis:	Treatment emmean SE df asymp.LCL asymp.UCL .group ammonium 0.0310 0.002035 Inf 0.02646 0.0356 a nitrate 0.0313 0.002056 Inf 0.02673 0.0359 a	Position = 14, Tissue = cortex:	Treatment emmean SE df asymp.LCL asymp.UCL .group ammonium 0.0437 0.002867 Inf 0.03727 0.0501 a nitrate 0.0420 0.002756 Inf 0.03582 0.0481 a
15. Position = 15, Tissue = epidermis:	Treatment emmean SE df asymp.LCL asymp.UCL .group ammonium 0.0277 0.001820 Inf 0.02366 0.0318 a nitrate 0.0302 0.001982 Inf 0.02576 0.0346 a	Position = 15, Tissue = cortex:	Treatment emmean SE df asymp.LCL asymp.UCL .group ammonium 0.0403 0.002647 Inf 0.03441 0.0462 a nitrate 0.0421 0.002761 Inf 0.03590 0.0482 a
16. Position = 16, Tissue = epidermis:	Treatment emmean SE df asymp.LCL asymp.UCL .group ammonium 0.0233 0.001530 Inf 0.01989 0.0267 a nitrate 0.0252 0.001652 Inf 0.02148 0.0289 a	Position = 16, Tissue = cortex:	Treatment emmean SE df asymp.LCL asymp.UCL .group ammonium 0.0370 0.002427 Inf 0.03156 0.0424 a nitrate 0.0394 0.002588 Inf 0.03365 0.0452 a
17. Position = 17, Tissue = epidermis:	Treatment emmean SE df asymp.LCL asymp.UCL .group ammonium 0.0212 0.001390 Inf 0.01806 0.0243 a nitrate 0.0256 0.001731 Inf 0.02176 0.0295 b	Position = 17, Tissue = cortex:	Treatment emmean SE df asymp.LCL asymp.UCL .group ammonium 0.0350 0.002168 Inf 0.02818 0.0379 a nitrate 0.0373 0.002448 Inf 0.03182 0.0428 a
18. Position = 18, Tissue = epidermis:	Treatment emmean SE df asymp.LCL asymp.UCL .group ammonium 0.0176 0.001157 Inf 0.01504 0.0202 a nitrate 0.0241 0.001676 Inf 0.02032 0.0278 b	Position = 18, Tissue = cortex:	Treatment emmean SE df asymp.LCL asymp.UCL .group ammonium 0.0310 0.002033 Inf 0.02643 0.0355 a nitrate 0.0332 0.002179 Inf 0.02832 0.0381 a
19. Position = 19, Tissue = epidermis:	Treatment emmean SE df asymp.LCL asymp.UCL .group ammonium 0.0127 0.000944 Inf 0.01057 0.0148 a nitrate 0.0253 0.001954 Inf 0.02094 0.0297 b	Position = 19, Tissue = cortex:	Treatment emmean SE df asymp.LCL asymp.UCL .group ammonium 0.0298 0.002075 Inf 0.02517 0.0345 a nitrate 0.0293 0.001921 Inf 0.02497 0.0336 a
20. Position = 20, Tissue = epidermis:	Treatment emmean SE df asymp.LCL asymp.UCL .group ammonium 0.0104 0.000870 Inf 0.00842 0.0123 a nitrate 0.0218 0.001685 Inf 0.01805 0.0256 b	Position = 20, Tissue = cortex:	Treatment emmean SE df asymp.LCL asymp.UCL .group ammonium 0.0278 0.002066 Inf 0.02314 0.0324 a nitrate 0.0254 0.001669 Inf 0.02170 0.0292 a

C.



946

947 **Supplementary Document 1. Statistical reasoning.**

948 **A.** Estimated marginal mean (EMM) comparisons of cell lengths in different tissues (epidermis  
 949 vs cortex) at each cell position (1-20 from QC) for each treatment (ammonium vs nitrate)  
 950 applied on a generalized linear model (GLM). Significant differences ( $p < 0.01$ ) are highlighted  
 951 in red. **B.** EMM comparisons of cell lengths in different treatments (ammonium vs nitrate) at  
 952 each cell position (1-20 from QC) for epidermis vs cortex on the same GLM model. Significant  
 953 differences ( $p < 0.01$ ) are highlighted in red. **C.** A decision tree based on recursive partitioning  
 954 analysis shows the hierarchical importance of each treatment, tissue and cell position variable  
 955 on cell length differences.

956

957 **Methods**

958 **Plant material**

959 *Arabidopsis thaliana* (L.) Heynh plants were used in this work. The transgenic lines *WI31Y*<sup>67</sup>,  
 960 *PIN2::PIN2-GFP*<sup>68</sup> in *eir1-4* background, *PIN2::PIN2S439D-GFP*, *PIN2::PIN2S439A-GFP*  
 961 (Vega et al.,) were introduced into *eir1-4* background; *PIN2::PIN2-Dendra*<sup>69</sup>, *R2D2*<sup>70</sup>, *DII-*  
 962 *VENUS*<sup>70</sup>, *mDII-VENUS*<sup>70</sup>, *PIN2::nls-GFP*<sup>71</sup>, *DR5::LUC*<sup>72</sup>, *DR5::RFP*<sup>73</sup>, *CyclinB1::GUS*<sup>74</sup>  
 963 and the T-DNA mutant line *eir1-4* were described previously. *DII-VENUS* and *mDII-VENUS*  
 964 in *eir1-4* background lines were obtained by manual hand pollination of the individual lines.

965 **Growth conditions**

966 Seeds of *A. thaliana* were surface-sterilized by 70% ethanol and sown on a modified Murashige  
967 and Skoog (MS) medium - Boric Acid 6.2 mg/L, Calcium Chloride (anhydrous) 332.2 mg/L,  
968 Cobalt Chloride (6H<sub>2</sub>O) 0.025 mg/L, Cupric Sulfate (5H<sub>2</sub>O) 0.025 mg/L, Na<sub>2</sub>EDTA (2H<sub>2</sub>O)  
969 37.26 mg/L, Ferrous Sulfate (7H<sub>2</sub>O) 27.8 mg/L, Magnesium Sulfate (anhydrous)180.7 mg/L,  
970 Molybdic Acid (disodium salt 2H<sub>2</sub>O) 0.25 mg/L, Potassium Iodide 0.83 mg/L, Potassium  
971 Phosphate (monobasic, anhydrous) 170 mg/L, Zinc Sulfate (7H<sub>2</sub>O) 8.6 mg/L – which contained  
972 0.5mM Ammonium Succinate (Santa Cruz Biotechnology) (76 mg/L) as a nitrogen source and  
973 supplemented with 0.1% sucrose and 1% agar (Type E, Sigma A4675), pH=5,8. The nitrate  
974 amended media contained 5mM Potassium Nitrate (505 mg/L) instead of 0.5mM Ammonium  
975 Succinate. Seeds were stratified at least for 3 d and grown for 4-14 d at 21 °C in a 16 h light/8  
976 h dark cycle.

### 977 **Root growth and root length analysis**

978 7-day-old light-grown seedlings were transferred to either ammonium or nitrate amended plates  
979 and scanned on a daily basis for 7 days on an Epson Perfection V700 flatbed scanner. Root  
980 growth (root length changes over a given period of time) and root length were measured  
981 manually using Fiji (v1.52).

### 982 **Cell elongation and cell length analysis**

983 Cell elongation was measured after 12 hours exposure to either to ammonium or nitrate  
984 manually with the software Fiji (v1.52).

985 For cell length analysis, confocal microscopic images of propidium iodide-stained  
986 *PIN2::PIN2-GFP*, *PIN2::PIN2S439A-GFP*, *PIN2::PIN2S439D-GFP*, Col-0 and *eir1-4* roots  
987 were used and the length of each cell in different cell files (epidermis and cortex) was measured  
988 manually using Fiji (v1.52).

### 989 **Imaging and image analysis**

990 5 DAG seedlings were mounted on a slice of MS medium - containing either 0.5mM  
991 ammonium or 5mM nitrate - placed into a chambered coverslip (Lab-Tek) and imaged with  
992 Zeiss LSM700, LSM800 or LSM880 inverted confocal microscopes equipped either with a  
993 20×/0.8 Plan-Apochromat M27 objective or a 40× Plan-Apochromat water immersion  
994 objective. Fluorescence signals for GFP (excitation 488 nm, emission 507 nm), YFP (excitation  
995 514 nm, emission 527 nm), PI (excitation 536 nm, emission 617 nm) and DAPI (excitation 405  
996 nm, emission 461 nm) were detected. A LaVision 2-Photon Inverted TriM Scope II from  
997 LaVision Biotec with a FLIM X16 TCSPC detector from LaVision Biotec equipped with a  
998 Olympus UApo N340 40xW, NA 1.15 was also used. Roots were observed 12 hours after

999 transfer to ammonium or nitrate supplemented media. Long time-lapse imaging was performed  
1000 using a vertically oriented LSM700 microscope as described previously<sup>32</sup>.

1001 For image quantification (R2D2, DII-Venus, mDII-Venus, PIN2-GFP fluorescence intensity  
1002 measurements), maximum intensity projections of confocal pictures were used. Images were  
1003 handled and analysed with Fiji (v1.52) and Adobe Photoshop (Adobe Creative Cloud).

#### 1004 **PIN2-DENDRA photoconversion and FRAP experiments**

1005 PIN2-DENDRA experiments were executed as previously described<sup>71</sup>. Briefly,  
1006 photoconversion of 5 DAG seedlings expressing *PIN2-Dendra* into its red form induced by  
1007 illuminating the region of interest with UV light and the depletion of the red and re-appearance  
1008 of the green signals in ammonium or nitrate transferred *Arabidopsis* roots was followed over  
1009 time using a vertically oriented LSM700 microscope. Observation of roots initiated 10-20  
1010 minutes after transfer and images were recorded every 20 minutes (9 stacks/root/ recording).  
1011 The experiment was repeated 3 times and each experiment consisted of imaging 6 roots per  
1012 condition. Image analysis was performed using Fiji (v1.52). Red and green fluorescent signal  
1013 changes were measured on 10-10 individual cell membranes in the TZ over a period of 6 hours.  
1014 FRAP experiments were performed as described previously<sup>75</sup>. Briefly, individual membranes  
1015 of 5 DAG old *PIN2-GFP* expressing *Arabidopsis* roots transferred either to ammonium or  
1016 nitrate were bleached using the 488nm laser of a Zeiss LSM800 confocal microscope according  
1017 to its built-in bleaching protocol. Recovery of the PIN2-GFP signal at the bleached areas was  
1018 followed for 10 minutes and quantification of fluorescence recovery was measured using Fiji  
1019 (v1.52).

#### 1020 **PIN2 immunodetection and staining of nuclei**

1021 For PIN2 immunostaining, 5 DAG *Arabidopsis* roots were handled as previously described<sup>76</sup>.  
1022 Briefly, fixation was performed using 2% PFA (in 1xMTSB) supplemented with 0.1 %  
1023 TritonX-100, followed by hydrophilisation using MeOH 100 % (65°C, 10 minutes), cell wall  
1024 digestion using 0.2 % Driselase and 0.15 % Macerozyme in 2 mM MES, pH 5.0 (37°C, 40  
1025 minutes), and membrane permeabilisation using 3% NP-40, 10 % DMSO in 1× MTSB (37°C,  
1026 20 minutes). Anti-PIN2 (1:100) was used as a primary antibody (37°C, 120 minutes). Alexa  
1027 Fluor 488 goat anti-rabbit IgG H+L (Thermo Fischer Scientific) was used as secondary  
1028 antibody (1:800) (37°C, 60 minutes). Finally, samples were mounted in VECTASHIELD®  
1029 Antifade Mounting Medium with DAPI (4',6-Diamidino-2-Phenylindole, Dihydrochloride).  
1030 Images were obtained using an LSM800 microscope.



1031 **Quantification of R2D2, DII-VENUS and mDII-VENUS fluorescence signal in**  
1032 ***Arabidopsis* roots**

1033 *R2D2* combines *RPS5A*-driven *DII* (*DII* domain of the *INDOLE-3-ACETIC ACID28* (*IAA28*,  
1034 *DII*) from *Arabidopsis*) fused to  $n3 \times Venus$  and *RPS5A*-driven *mDII* fused to *ntdTomato* on a  
1035 single transgene<sup>40,46</sup>. *DII-VENUS* is the domain II of *IAA28* fused to the *VENUS* fast maturing  
1036 *YFP* and *mDII-VENUS* is the non-degradable form of *DII-VENUS*. The analysis of the  
1037 fluorescence intensity of either *R2D2*, *DII-VENUS* or *mDII-VENUS* expressing plants grown  
1038 on ammonium containing and transferred on ammonium and nitrate containing medium was  
1039 performed on Maximum Intensity Projection of *Z*-stacks of root tips acquired with a Zeiss LSM  
1040 700 inverted laser-scanning microscope as described in<sup>60</sup> with slight modifications.

1041 To quantify the fluorescence signal in each cell per selected root tissue (epidermis and cortex)  
1042 first we positioned a segmented line over the nuclei in the corresponding tissues with the ROI  
1043 manager tool of the software Fiji (v1.52) (Supplemental Fig 3C). Next, we analyzed the  
1044 fluorescence plot profiles of the different lines with the peak analyzer function of the software  
1045 Origin (OriginLab Corporation) to find local maxima along the lines, which represented the  
1046 fluorescence value of the nuclei in the tissues. In case of *R2D2*, auxin distribution plots were  
1047 derived by reciprocal mean values of the normalized  $n3xVenus/ntdTomato$  ratio. Relative  
1048 auxin level data in each cell per tissue were graphed after data interpolation using the Origin  
1049 built-in algorithm for smoothing.

1050 **3D SIM and Polar Density Analysis of PIN2-GFP**

1051 Live *Arabidopsis* seedlings, which were incubated on either nitrate or ammonium amended  
1052 medium for 6-8 hours, were mounted on to coverslips as previously described by Johnson and  
1053 Vert<sup>77</sup> with the coverslips additionally fixed to the slide with nail polish. Cells in the elongation  
1054 zone of the root epidermis were imaged using an OMX BLAZE v4 3D SIM (Applied  
1055 Precision), as described<sup>78</sup>. Briefly, a 60x 1.42 NA Oil Immersion objective and a 100 mW 488  
1056 laser was used to make optical sections in the *Z* dimension, in order to capture the totality of  
1057 the lateral polar domain of the subject cell. Each *Z*-section image is based on 15 images  
1058 generated from 3 different angles and 5 different SIM patterns and reconstructed using  
1059 SOFTWORX software (Applied Precision).

1060 A maximum projection of the *Z*-stack was used for analysis. Images were made binary and  
1061 subjected to watershed segmentation using Fiji<sup>79</sup>. *PIN2* spots were then detected using  
1062 TrackMate<sup>80</sup>. The number of *PIN2* spots was calculated in regions of interest (0.8 microns in

1063 width times the height of the cell) at distances sequentially further away from the polar end of  
1064 the cell using a custom made Matlab script. The raw number of spots in each ROI was then  
1065 normalised and plotted.

### 1066 **Quantification of LUCIFERASE (LUC) activity in *Arabidopsis* roots**

1067 *DR5::LUC* expressing 7 DAG *Arabidopsis* seedlings were transferred to ammonium or nitrate  
1068 containing agar plates and roots (40 roots per treatment per time point) were collected after 1  
1069 and 6 HAT and snap frozen in liquid nitrogen. Frozen root tissue was extracted in Reporter  
1070 Lysis Buffer (Promega) and LUC activity was measured with the Luciferase Assay Reagent  
1071 (Promega) in a multiwell plate in a Biotek SynergyH1 platereader.

### 1072 **Measurements of basipetal (shootward) auxin transport in *Arabidopsis* roots**

1073 The shootward transport assay of [3H]-IAA in *Arabidopsis* roots was performed according to  
1074 a previous report<sup>81</sup>, with a few modifications. 7 DAG Col-0 or *eir1-4* seedlings were transferred  
1075 to ammonium, nitrate or MS (Murashige Skoog Basal Medium) medium with 15 seedlings as  
1076 one biological replicate, and 3 replicates per treatment. The [3H]-IAA (PerkinElmer, ART-  
1077 0340) droplets were prepared in MS medium with 1.25% agar and 500 mM [3H]-IAA (1.45  
1078 mL in 10 mL) and were carefully placed on the root meristem (at the very end of the roots).  
1079 After incubation for 6 hours in the dark, the part of the root which was covered by the droplet  
1080 was cut, the remaining root parts were collected and ground completely in liquid nitrogen and  
1081 homogenized in 1 mL scintillation solution (PerkinElmer, 6013199). The samples were  
1082 incubated overnight to allow the radioactivity to evenly diffuse into the whole volume of the  
1083 scintillation cocktail. Finally the radioactivity was measured with a scintillation counter (Hidex  
1084 300XL), with each sample counted for 100 s, 3 times. 3 samples with only the scintillation  
1085 solution were used as background controls. As an additional background control another batch  
1086 of samples were prepared the same way as described above except [3H]-IAA containing  
1087 droplets were placed not on the root meristem but next to the seedlings. Data shown on the  
1088 figure was calculated against the background.

### 1089 **GUS ( $\beta$ -Glucuronidase) staining**

1090 *CycB1::GUS* expression was analyzed in seedling roots 7 DAG, 12 HAT to ammonium or  
1091 nitrate containing media. Seedlings were incubated for 2 hours in 37°C in staining buffer  
1092 containing 1mM ferricyanide, 150 mM sodium phosphate buffer (pH 7) and 1mg/ml of X-Gluc  
1093 dissolved in DMSO. Seedlings were cleared using subsequent incubation at room temperature  
1094 in a series of ethanol dilutions from 60% to 10% then mounted on slides with 5% ethanol-  
1095 50% glycerol mounting solution. The pattern of the GUS histochemical staining was analyzed

1096 by an Olympus BX53 microscope and Olympus DP26 digital camera, controlled by cellSense  
1097 Entry software.

### 1098 **RT-qPCR analysis**

1099 Total RNA was extracted from excised 7 DAG roots 1, 6 and 48 HAT to ammonium or nitrate  
1100 amended plates using RNeasy® Plant Mini kit (QIAGEN) according to the manufacturer's  
1101 protocol. 1µg of RNA was used to synthesize cDNA using iScript™ cDNA synthesis kit (Bio-  
1102 Rad). The analysis was carried out on a LightCycler 480 II (SW1.5.1 Version; Roche  
1103 Diagnostics) with the SYBR Green I Master kit (Roche Diagnostics) according to the  
1104 manufacturer's instructions. All PCR reactions were carried out with biological and technical  
1105 triplicates. Expression levels of target genes were quantified by specific primers that were  
1106 designed using Quant Prime<sup>82</sup>, and validated by performing primer efficiency for each primers  
1107 pair. The levels of expression of each gene were first measured relative to *AT4G05320*  
1108 (*UBQ10*) and then to respective mock treatment.

Gene	Transcript Identifier	Primer FW	Primer REV
<i>AT4G05320</i>	<i>UBQ10</i>	<i>CACACTCCACTTGGTCTTGC</i>	<i>TGGTCTTTCCGGTGAGAGTCTCA</i>
<i>PIN2</i>	<i>AT5G57090.1</i>	<i>TCACGACAACCTCGCTACTAAAGC</i>	<i>TGCCCATGTAAGGTGACTTTCCC</i>
<i>ANR1</i>	<i>AT2G14210.1</i>	<i>AAGAGGAGCAGCATCAACTTCTG</i>	<i>TCCTCTCCCCTAGTTTCCTGTG</i>

### 1109 **Reproducibility and statistics**

1110 The number of independent repetitions of experiments, as well as exact sample sizes, is  
1111 described in the figure legends. Statistical analysis (t-test and ANOVA) were performed using  
1112 the software Origin (v2018). Statistical significance was tested as described in the figure  
1113 legends.

1114 For the regression analysis in supplementary document 1, Col-0 cell length measurements were  
1115 analyzed together with associated categorical variables represented by plant sample of origin  
1116 (n=18), tissue (n=2, i.e. epidermis and cortex), cell position (n=20) and treatment (n=2, i.e.  
1117 NO<sub>3</sub><sup>-</sup> and NH<sub>4</sub><sup>+</sup>). The importance of the variables was initially assessed via Random Forest  
1118 analysis in R (v 1.2.5033). A machine learning training was conducted with the caret R  
1119 package<sup>83</sup> for tuning the Random Forest and the best mtry parameter was selected according to  
1120 Root Mean Square Error (RMSE) and R-squared (R<sup>2</sup>) measures in R. Data distribution,  
1121 skewness and kurtosis were checked with the fitdistrplus R package<sup>84</sup> and Gamma distribution

1122 was chosen for setting up a regression analysis based on generalized linear models (GLMs).  
1123 Besides the main effects of the variables, several models were virtually possible when the  
1124 interactions between some or all the variables were considered. First, a simple model including  
1125 only main effects was generated and residual vs. fitted values evaluated prior to analysis of  
1126 deviance. Second, a model including main effects and all possible interactions between  
1127 variables was built. The analysis of the interactions of the fit model was carried out with the  
1128 *phia* R package<sup>85</sup>, showing a possible but not strong interaction between tissue and treatment  
1129 factors. This insight was used to generate a third model. The performance of the second and  
1130 third model was then compared by repeated k-fold cross-validation with the *caret* R package  
1131 and the second model was selected according to RMSE and R<sup>2</sup> measures. After analysis of  
1132 deviance, post hoc pairwise comparisons were conducted with estimated marginal means  
1133 (EMMs) using the *emmeans* R package<sup>86</sup> (Supplemental Document 1a-b). A recursive  
1134 partitioning analysis was performed and a decision tree was generated with the *partykit* R  
1135 package<sup>87</sup> to confirm the results showed by regression analysis and to visualize the role of  
1136 different variables on cell length distribution (Supplemental Document 1c).

## 1137 **Computational methods**

### 1138 *Visualization of model predictions*

1139 The computer simulation representing the dynamic auxin flow through the root tissues was  
1140 created using the version of VV (Vertex-Vertex) programming language and in the L-system-  
1141 based modeling software L-studio<sup>88</sup>. The model simulates a cross-section of the plant root  
1142 focusing on the cortical and epidermal tissues. Plant cells are visualized as four-sided polygons  
1143 representing the cell walls. For the sake of simplicity, cell membranes and the extracellular  
1144 space shared by adjacent cells are not rendered. Only the first ~20 cells (counting from the QC)  
1145 are visualized, mirroring the available experimental measurements. Meristematic and  
1146 elongating cells are distinguished with different cell wall coloring; blue for meristem and  
1147 yellow for elongation zone, respectively. Auxin is represented as filled green circles inside  
1148 each cell, the radius of the circle proportional to the size of the cell indicates the amount of  
1149 auxin present in that cell. PIN2 protein localization on the PM is represented as red dots close  
1150 to the cell walls; PIN2 can be apical (shootward), basal (rootward) or lateral (outer). Despite  
1151 being taken into account for mathematical calculations, cytoplasmic accumulation of PIN2 is  
1152 not shown in the model visualizations. Our model enables dynamic simulation of root growth,  
1153 elongation and auxin flow through the root apex. Individual cells grow, elongate and  
1154 consequently divide. Auxin is pumped across cell walls through the ATP-dependent action of

1155 PIN2 proteins on the cell membrane. Auxin that reaches the outer limit of the tissues is simply  
 1156 removed from the system. PIN2 is expressed, trafficked and degraded according to the model  
 1157 rules described in the following sections.

### 1158 ***Mathematical model description***

1159 The model assumes that the epidermis contributes to an active passage auxin into deeper  
 1160 tissues. Two main sources of auxin into the epidermis were considered:

- 1161 1) The cell that is closest to the QC, which is known to be a main source of auxin production<sup>89</sup>.
- 1162 2) The lateral root cap, which due to its structural conformation force the influx of auxin into  
 1163 the initial cells of the epidermis<sup>90</sup>.

1164 The ordinary differential equation describing auxin dynamic in a single cell  $i$  is:

$$1165 \quad \frac{dA_i}{dt} = (s_1 \cdot i < z + s_2 \cdot i \geq z) + \sum_{j=1}^n k_a (A_j PIN_j - A_i PIN_i) - d_a A_i$$

1166 Where  $s_1$  and  $s_2$  denote the two auxin sources into the epidermis), while  $z$  indicates the cell  
 1167 location of the LRC-derived auxin influx (cell number 20 from the QC).  $k_a$  represents the rate  
 1168 of active auxin transport between cells via PIN2. The exchange of auxin occurs for each cell  $j$   
 1169 connected to cell  $i$ . General processes of auxin degradation like conjugation and oxidation are  
 1170 summarized by a single degradation rate,  $d_a$ .

1171 PIN2 is the only auxin efflux carries considered in this model. High auxin concentrations lead  
 1172 to an increased degradation of PIN proteins<sup>48,91</sup>. We modeled the effect of auxin on cytoplasmic  
 1173 PIN2 inside cell  $i$  by approximating functional forms, in what follow:

$$1174 \quad \frac{dPIN_{ci}}{dt} = m_p - d_p PIN_{ci} \cdot \left( 1 + \frac{A_i}{q_p} \right)$$

1175 The expression parameter  $m_p$  indicates the basal rate of PIN2 protein synthesis. PIN2  
 1176 degradation is modeled over a constant rate of degradation,  $d_p$ , which increases linearly  
 1177 according to auxin levels by  $q_p$ .

1178 PIN2 trafficking to the apical/basal membranes is modeled as follows:

$$1179 \quad \frac{dPIN_{mi}}{dt} = PIN_{ci} (1 - l_n) \left( (tr_n + tr_{wn}) \cdot (1 - tr_n + tr_{wn}) \right) \cdot Logistic (tr_a A_i + tr_i i)$$

1180 The amount of PIN2 on the membrane  $m$  of cell  $i$  is regulated by the basal trafficking rates on  
 1181  $\text{NO}_3^-$  ( $tr_n$ ) or  $\text{NH}_4^+$  ( $tr_{wn}$ ), which in turn is allowed to saturate to zero or to the maximum rate  
 1182 depending on the level of auxin and the distance from the QC, according to logistic coefficients  
 1183  $tr_a$  and  $tr_i$ , respectively.  $l_n$  represents the percentage of PIN2 that is redirected to the lateral  
 1184 membranes, depending on nitrate levels. In this model, nitrate level is represented as a binary  
 1185 variable:  $\text{NO}_3^-$  for nitrate supplement and 0 for  $\text{NH}_4^+$  supplement.

1186 Cell division is regulated though a hypothetical division factor as proposed in a previous  
 1187 study<sup>92</sup>. The concentration of division factor in a single cell  $i$  is describes as:

$$\frac{dDIV_i}{dt} = k_{v0} \cdot \frac{\left(k_{v1} \cdot \frac{A_i}{\max A}\right) + \left(\frac{len_i}{\max L}\right)}{1 + e^{(i \cdot t_v)}} - DIV_i \cdot k_{v2} \frac{1 + \left(\frac{A_i}{k_{v3}}\right)^{h_1}}{1 + \left(\frac{A_i}{k_{v4}}\right)^{h_2}}$$

1188

1189 Where  $k_{v0}$  denotes the maximal synthesis rate of division factor;  $len_i$  and  $\max L$  the length of  
 1190 cell  $i$  and the maximum cell length achievable, respectively;  $t_v$  is the tolerance factor restricting  
 1191 the location in the meristem where division takes place;  $k_{v1}$  is the level of auxin-dependent  
 1192 division factor activation. The right part of the formula describes the hypothesized process of  
 1193 division factor degradation, where  $k_{v2}$  is the degradation rate of the division factor;  $k_{v3}$  and  $k_{v4}$   
 1194 are the level of auxin-dependent division factor activation and saturation, respectively;  $h_1$  and  
 1195  $h_2$  are hill's coefficient.

1196 Cell growth is an auxin-dependent mechanism and cell entrance in the elongation phase is  
 1197 triggered by an auxin concentration threshold. Both in the meristem and the elongation zone  
 1198 cell growth is defined as follow:

$$\frac{dL_i}{dt} = k_l \cdot \frac{A_i}{A_i + 1} L_i \cdot \left(1 - \frac{len_i}{m_l}\right)$$

1199

1200 Where  $k_l$  indicates the cell elongation rate (depending whether the cell in the meristem or in  
 1201 the elongation zone),  $len_i$  the cell length, and  $m_l$  the maximum length the cell can achieve  
 1202 (depending whether the cell in the meristem or in the elongation zone).

1203 ***Statistical inference and parameters estimation***



1204 Data analysis and plotting was performed using the R language environment for statistical  
1205 computing<sup>93</sup> and the plotting package ggplot<sup>94</sup>. Parameters estimation of the previously  
1206 described models was carried out with the RStan<sup>95</sup> and brms<sup>96</sup> packages, which implement a  
1207 modified version of Hamiltonian Monte Carlo sampling algorithm to approximate the  
1208 parameters posterior distribution. Model comparison was performed using the loo package<sup>97</sup> to  
1209 carry out Pareto smoothed importance-sampling leave-one-out cross-validation (PSIS-LOO)  
1210 for posterior predictive performance estimation.

### 1211 *Auxin source implementation and testing*

1212 To test auxin source impact on the model predictions we considered four possible scenarios  
1213 (Supplementary Fig. 10f):

1214 1) Model A: A naive model assuming a uniform source of auxin along the epidermis (uniform  
1215 source)

1216 2) Model B: The current model that consider two separate sources from the QC and the LRC  
1217 (LRC source)

1218 3) Model C: A highly complex model that assume input source modeled as a versatile spline  
1219 (spline source)

1220 4) Model D: A more complex but less realistic model allowing for different input of auxin for  
1221 each epidermis cell (multiple point source)

1222 To identify the best model, we tested Models A-D against experimental measurements and  
1223 generate the information criteria based on the expected log probability density (Supplementary  
1224 Fig. 10f). A lowest information criterion was found for Model B as indicated the posterior  
1225 predictive performance, thereby Model B was used for the further study. We decided to  
1226 exclude the existence of a significant influx of auxin into the cortical cells; this was backed by  
1227 previous researches which suggested that at high auxin levels endodermal cells have the  
1228 tendency to lateralize toward the internal tissues and not toward the cortex<sup>98</sup>.

### 1229 *Parameters values used in the model*

1230 Parameters values used in the model are listed below with their estimated mean and  
1231 lower/upper 95% credible intervals.

Parameter	Mean	l-95% CI	u-95% CI	Reference (when not estimated from data)
$d_a / k_a$	<b>0.018</b>	<b>0.018</b>	<b>0.018</b>	<sup>92</sup>
$s_1$	<b>8.36</b>	<b>0.44</b>	<b>21.54</b>	-
$s_2$	<b>22.53</b>	<b>9.13</b>	<b>36.46</b>	-
$z$	<b>10.6</b>	<b>8.39</b>	<b>12.02</b>	-
$m_p$	<b>30.49</b>	<b>16.69</b>	<b>46.00</b>	-
$d_p$	<b>0.065</b>	<b>0.051</b>	<b>0.079</b>	-
$q_p$	<b>100</b>	<b>100</b>	<b>100</b>	<sup>99</sup>
$l_n$	<b>0.60</b>	<b>0.51</b>	<b>0.69</b>	-
$tr_n$	<b>0.246</b>	<b>0.226</b>	<b>0.267</b>	-
$tr_{wn}$	<b>0.13</b>	<b>0.11</b>	<b>0.15</b>	-
$tr_a$	<b>-0.05</b>	<b>-0.10</b>	<b>-0.00</b>	-
$tr_i$	<b>0.30</b>	<b>0.25</b>	<b>0.34</b>	-
$k_{v0}$	<b>1.5</b>	<b>1.5</b>	<b>1.5</b>	<sup>92</sup>
$k_{v1}$	<b>20</b>	<b>20</b>	<b>20</b>	<sup>92</sup>
$k_{v2}$	<b>0.3</b>	<b>0.3</b>	<b>0.3</b>	<sup>92</sup>
$k_{v3}$	<b>3.5</b>	<b>3.5</b>	<b>3.5</b>	<sup>92</sup>
$k_{v4}$	<b>0.5</b>	<b>0.5</b>	<b>0.5</b>	<sup>92</sup>
$t_v$	<b>0.1</b>	<b>0.1</b>	<b>0.1</b>	<sup>92</sup>
$h_1$	<b>2</b>	<b>2</b>	<b>2</b>	<sup>92</sup>
$h_2$	<b>3</b>	<b>3</b>	<b>3</b>	<sup>92</sup>
$k_l$	<b>0.3</b>	<b>0.2</b>	<b>0.4</b>	<sup>100</sup>
$m_l$	<b>200</b>	<b>150</b>	<b>250</b>	<sup>79</sup>

1232

1233

### 1234 References

- 1235 1. López-Bucio, J., Cruz-Ramírez, A. & Herrera-Estrella, L. The role of nutrient availability in  
1236 regulating root architecture. *Curr. Opin. Plant Biol.* **6**, 280–287 (2003).
- 1237 2. Marhava, P. *et al.* Re-activation of Stem Cell Pathways for Pattern Restoration in Plant Wound  
1238 Healing. *Cell* **177**, 957-969.e13 (2019).
- 1239 3. Fendrych, M., Leung, J. & Friml, J. TIR1/AFB-Aux/IAA auxin perception mediates rapid cell wall  
1240 acidification and growth of Arabidopsis hypocotyls. *eLife* **5**, (2016).

- 1241 4. Marschner, H. *Mineral nutrition of higher plants*. (Acad. Press, 2008).
- 1242 5. von Wirén, N., Gazzarrini, S. & Frommer, W. B. Regulation of mineral nitrogen uptake in plants.  
1243 *Plant Soil* **196**, 191–199 (1997).
- 1244 6. Jia, Z. & Wirén, N. von. Signaling pathways underlying nitrogen-dependent changes in root  
1245 system architecture: from model to crop species. *J. Exp. Bot.* (2020) doi:10.1093/jxb/eraa033.
- 1246 7. Waidmann, S., Sarkel, E. & Kleine-Vehn, J. Same same, but different: growth responses of  
1247 primary and lateral roots. *J. Exp. Bot.* (2020) doi:10.1093/jxb/eraa027.
- 1248 8. Gruber, B. D., Giehl, R. F. H., Friedel, S. & Wirén, N. von. Plasticity of the Arabidopsis Root  
1249 System under Nutrient Deficiencies. *Plant Physiol.* **163**, 161–179 (2013).
- 1250 9. Forde, B. G. Nitrogen signalling pathways shaping root system architecture: an update. *Curr.*  
1251 *Opin. Plant Biol.* **21**, 30–36 (2014).
- 1252 10. Giehl, R. F. H. & Wirén, N. von. Root Nutrient Foraging. *Plant Physiol.* **166**, 509–517 (2014).
- 1253 11. Remans, T. *et al.* The Arabidopsis NRT1.1 transporter participates in the signaling pathway  
1254 triggering root colonization of nitrate-rich patches. *Proc. Natl. Acad. Sci.* **103**, 19206–19211  
1255 (2006).
- 1256 12. Lima, J. E., Kojima, S., Takahashi, H. & von Wirén, N. Ammonium triggers lateral root branching  
1257 in Arabidopsis in an AMMONIUM TRANSPORTER1;3-dependent manner. *Plant Cell* **22**, 3621–  
1258 3633 (2010).
- 1259 13. Fredes, I., Moreno, S., Díaz, F. P. & Gutiérrez, R. A. Nitrate signaling and the control of  
1260 Arabidopsis growth and development. *Curr. Opin. Plant Biol.* **47**, 112–118 (2019).
- 1261 14. Guan, P. Dancing with Hormones: A Current Perspective of Nitrate Signaling and Regulation in  
1262 Arabidopsis. *Front. Plant Sci.* **8**, 1697 (2017).
- 1263 15. Ristova, D. *et al.* Combinatorial interaction network of transcriptomic and phenotypic responses  
1264 to nitrogen and hormones in the Arabidopsis thaliana root. *Sci. Signal.* **9**, rs13 (2016).
- 1265 16. Krouk, G. Hormones and nitrate: a two-way connection. *Plant Mol. Biol.* **91**, 599–606 (2016).

- 1266 17. Chen, F. *et al.* Evaluation of the yield and nitrogen use efficiency of the dominant maize hybrids  
1267 grown in North and Northeast China. *Sci. China Life Sci.* **56**, 552–560 (2013).
- 1268 18. Tian, Q., Chen, F., Liu, J., Zhang, F. & Mi, G. Inhibition of maize root growth by high nitrate supply  
1269 is correlated with reduced IAA levels in roots. *J. Plant Physiol.* **165**, 942–951 (2008).
- 1270 19. Caba, J. M., Centeno, M. L., Fernández, B., Gresshoff, P. M. & Ligeró, F. Inoculation and nitrate  
1271 alter phytohormone levels in soybean roots: differences between a supernodulating mutant and  
1272 the wild type. *Planta* **211**, 98–104 (2000).
- 1273 20. Tamaki, V. & Mercier, H. Cytokinins and auxin communicate nitrogen availability as long-  
1274 distance signal molecules in pineapple (*Ananas comosus*). *J. Plant Physiol.* **164**, 1543–1547  
1275 (2007).
- 1276 21. Krouk, G. *et al.* Nitrate-regulated auxin transport by NRT1.1 defines a mechanism for nutrient  
1277 sensing in plants. *Dev. Cell* **18**, 927–937 (2010).
- 1278 22. Ma, W. *et al.* Auxin biosynthetic gene TAR2 is involved in low nitrogen-mediated reprogramming  
1279 of root architecture in *Arabidopsis*. *Plant J. Cell Mol. Biol.* **78**, 70–79 (2014).
- 1280 23. Walch-Liu, P., Liu, L.-H., Remans, T., Tester, M. & Forde, B. G. Evidence that L-glutamate can act  
1281 as an exogenous signal to modulate root growth and branching in *Arabidopsis thaliana*. *Plant*  
1282 *Cell Physiol.* **47**, 1045–1057 (2006).
- 1283 24. Gutiérrez, R. A. *et al.* Qualitative network models and genome-wide expression data define  
1284 carbon/nitrogen-responsive molecular machines in *Arabidopsis*. *Genome Biol.* **8**, R7 (2007).
- 1285 25. Gifford, M. L., Dean, A., Gutierrez, R. A., Coruzzi, G. M. & Birnbaum, K. D. Cell-specific nitrogen  
1286 responses mediate developmental plasticity. *Proc. Natl. Acad. Sci. U. S. A.* **105**, 803–808 (2008).
- 1287 26. Vidal, E. A. *et al.* Nitrate-responsive miR393/AFB3 regulatory module controls root system  
1288 architecture in *Arabidopsis thaliana*. *Proc. Natl. Acad. Sci. U. S. A.* **107**, 4477–4482 (2010).
- 1289 27. Vidal, E. A., Moyano, T. C., Riveras, E., Contreras-López, O. & Gutiérrez, R. A. Systems  
1290 approaches map regulatory networks downstream of the auxin receptor AFB3 in the nitrate  
1291 response of *Arabidopsis thaliana* roots. *Proc. Natl. Acad. Sci. U. S. A.* **110**, 12840–12845 (2013).

- 1292 28. Vidal, E. A. *et al.* Integrated RNA-seq and sRNA-seq analysis identifies novel nitrate-responsive  
1293 genes in *Arabidopsis thaliana* roots. *BMC Genomics* **14**, 701 (2013).
- 1294 29. Tsay, Y. F., Schroeder, J. I., Feldmann, K. A. & Crawford, N. M. The herbicide sensitivity gene  
1295 CHL1 of *Arabidopsis* encodes a nitrate-inducible nitrate transporter. *Cell* **72**, 705–713 (1993).
- 1296 30. Mounier, E., Pervent, M., Ljung, K., Gojon, A. & Nacry, P. Auxin-mediated nitrate signalling by  
1297 NRT1.1 participates in the adaptive response of *Arabidopsis* root architecture to the spatial  
1298 heterogeneity of nitrate availability. *Plant Cell Environ.* **37**, 162–174 (2014).
- 1299 31. Gifford, M. L. *et al.* Plasticity Regulators Modulate Specific Root Traits in Discrete Nitrogen  
1300 Environments. *PLoS Genet.* **9**, (2013).
- 1301 32. von Wangenheim, D. *et al.* Live tracking of moving samples in confocal microscopy for vertically  
1302 grown roots. *eLife* **6**, (2017).
- 1303 33. Yazdanbakhsh, N., Sulpice, R., Graf, A., Stitt, M. & Fisahn, J. Circadian control of root elongation  
1304 and C partitioning in *Arabidopsis thaliana*. *Plant Cell Environ.* **34**, 877–894 (2011).
- 1305 34. Baluska, F., Mancuso, S., Volkmann, D. & Barlow, P. W. Root apex transition zone: a signalling-  
1306 response nexus in the root. *Trends Plant Sci.* **15**, 402–408 (2010).
- 1307 35. Kong, X., Liu, G., Liu, J. & Ding, Z. The Root Transition Zone: A Hot Spot for Signal Crosstalk.  
1308 *Trends Plant Sci.* **23**, 403–409 (2018).
- 1309 36. Pavelescu, I. *et al.* A Sizer model for cell differentiation in *Arabidopsis thaliana* root growth. *Mol.*  
1310 *Syst. Biol.* **14**, (2018).
- 1311 37. Stepanova, A. N. *et al.* TAA1-mediated auxin biosynthesis is essential for hormone crosstalk and  
1312 plant development. *Cell* **133**, 177–191 (2008).
- 1313 38. Dello loio, R. *et al.* A genetic framework for the control of cell division and differentiation in the  
1314 root meristem. *Science* **322**, 1380–1384 (2008).
- 1315 39. Blilou, I. *et al.* The PIN auxin efflux facilitator network controls growth and patterning in  
1316 *Arabidopsis* roots. *Nature* **433**, 39–44 (2005).

- 1317 40. Liao, C.-Y. *et al.* Reporters for sensitive and quantitative measurement of auxin response. *Nat.*  
1318 *Methods* **12**, 207–210, 2 p following 210 (2015).
- 1319 41. Goldsmith, M. H. M. The Polar Transport of Auxin. *Annu. Rev. Plant Physiol.* **28**, 439–478 (1977).
- 1320 42. Adamowski, M. & Friml, J. PIN-dependent auxin transport: action, regulation, and evolution.  
1321 *Plant Cell* **27**, 20–32 (2015).
- 1322 43. Luschnig, C., Gaxiola, R. A., Grisafi, P. & Fink, G. R. EIR1, a root-specific protein involved in auxin  
1323 transport, is required for gravitropism in *Arabidopsis thaliana*. *Genes Dev.* **12**, 2175–2187 (1998).
- 1324 44. Müller, A. *et al.* AtPIN2 defines a locus of *Arabidopsis* for root gravitropism control. *EMBO J.* **17**,  
1325 6903–6911 (1998).
- 1326 45. Hanzawa, T. *et al.* Cellular Auxin Homeostasis under High Temperature Is Regulated through a  
1327 SORTING NEXIN1–Dependent Endosomal Trafficking Pathway[C][W]. *Plant Cell* **25**, 3424–3433  
1328 (2013).
- 1329 46. Brunoud, G. *et al.* A novel sensor to map auxin response and distribution at high spatio-temporal  
1330 resolution. *Nature* (2012) doi:10.1038/nature10791.
- 1331 47. Kleine-Vehn, J. *et al.* Recycling, clustering, and endocytosis jointly maintain PIN auxin carrier  
1332 polarity at the plasma membrane. *Mol. Syst. Biol.* **7**, 540 (2011).
- 1333 48. Kleine-Vehn, J. & Friml, J. Polar Targeting and Endocytic Recycling in Auxin-Dependent Plant  
1334 Development. *Annu. Rev. Cell Dev. Biol.* (2008) doi:10.1146/annurev.cellbio.24.110707.175254.
- 1335 49. Łangowski, Ł. *et al.* Cellular mechanisms for cargo delivery and polarity maintenance at different  
1336 polar domains in plant cells. *Cell Discov.* **2**, 16018 (2016).
- 1337 50. Barbosa, I. C. R., Hammes, U. Z. & Schwechheimer, C. Activation and Polarity Control of PIN-  
1338 FORMED Auxin Transporters by Phosphorylation. *Trends Plant Sci.* **23**, 523–538 (2018).
- 1339 51. Abas, L. *et al.* Intracellular trafficking and proteolysis of the *Arabidopsis* auxin-efflux facilitator  
1340 PIN2 are involved in root gravitropism. *Nat. Cell Biol.* **8**, 249–256 (2006).
- 1341 52. Baster, P. *et al.* SCFTIR1/AFB-auxin signalling regulates PIN vacuolar trafficking and auxin fluxes  
1342 during root gravitropism. *EMBO J.* **32**, 260–274 (2013).



- 1343 53. Tian, H., Niu, T., Yu, Q., Quan, T. & Ding, Z. Auxin gradient is crucial for the maintenance of root  
1344 distal stem cell identity in Arabidopsis. *Plant Signal. Behav.* **8**, (2013).
- 1345 54. Petersson, S. V. *et al.* An Auxin Gradient and Maximum in the Arabidopsis Root Apex Shown by  
1346 High-Resolution Cell-Specific Analysis of IAA Distribution and Synthesis. *Plant Cell* **21**, 1659–1668  
1347 (2009).
- 1348 55. Velasquez, S. M., Barbez, E., Kleine-Vehn, J. & Estevez, J. M. Auxin and cellular elongation. *Plant*  
1349 *Physiol.* (2016) doi:10.1104/pp.15.01863.
- 1350 56. Chapman, E. J. & Estelle, M. Cytokinin and auxin intersection in root meristems. *Genome Biol.*  
1351 (2009) doi:10.1186/gb-2009-10-2-210.
- 1352 57. Kong, X., Liu, G., Liu, J. & Ding, Z. The Root Transition Zone: A Hot Spot for Signal Crosstalk.  
1353 *Trends in Plant Science* (2018) doi:10.1016/j.tplants.2018.02.004.
- 1354 58. Jackson, R. B. & Caldwell, M. M. The Scale of Nutrient Heterogeneity Around Individual Plants  
1355 and Its Quantification with Geostatistics. *Ecology* **74**, 612–614 (1993).
- 1356 59. Nacry, P., Bouguyon, E. & Gojon, A. Nitrogen acquisition by roots: physiological and  
1357 developmental mechanisms ensuring plant adaptation to a fluctuating resource. *Plant Soil* **370**,  
1358 1–29 (2013).
- 1359 60. Di Mambro, R. *et al.* Auxin minimum triggers the developmental switch from cell division to cell  
1360 differentiation in the Arabidopsis root. *Proc. Natl. Acad. Sci. U. S. A.* **114**, E7641–E7649 (2017).
- 1361 61. Barbez, E., Dünser, K., Gaidora, A., Lendl, T. & Busch, W. Auxin steers root cell expansion via  
1362 apoplastic pH regulation in Arabidopsis thaliana. *Proc. Natl. Acad. Sci.* **114**, E4884–E4893 (2017).
- 1363 62. PNAS Plus: Auxin steers root cell expansion via apoplastic pH regulation in Arabidopsis thaliana.  
1364 <https://www.ncbi.nlm.nih.gov/pmc/articles/PMC5474774/>.
- 1365 63. Su, S.-H., Gibbs, N. M., Jancewicz, A. L. & Masson, P. H. Molecular Mechanisms of Root  
1366 Gravitropism. *Curr. Biol. CB* **27**, R964–R972 (2017).
- 1367 64. Zwiewka, M., Bilanovičová, V., Seifu, Y. W. & Nodzyński, T. The Nuts and Bolts of PIN Auxin Efflux  
1368 Carriers. *Front. Plant Sci.* **10**, (2019).

- 1369 65. Zhang, H. *et al.* Quantitative phosphoproteomics after auxin-stimulated lateral root induction  
1370 identifies an SNX1 protein phosphorylation site required for growth. *Mol. Cell. Proteomics MCP*  
1371 **12**, 1158–1169 (2013).
- 1372 66. Kumar, S., Stecher, G., Li, M., Knyaz, C. & Tamura, K. MEGA X: Molecular Evolutionary Genetics  
1373 Analysis across Computing Platforms. *Mol. Biol. Evol.* **35**, 1547–1549 (2018).
- 1374 67. Geldner, N. *et al.* Rapid, combinatorial analysis of membrane compartments in intact plants with  
1375 a multicolor marker set. *Plant J. Cell Mol. Biol.* **59**, 169–178 (2009).
- 1376 68. Vieten, A. *et al.* Functional redundancy of PIN proteins is accompanied by auxin-dependent  
1377 cross-regulation of PIN expression. *Dev. Camb. Engl.* **132**, 4521–4531 (2005).
- 1378 69. Jásik, J. *et al.* PIN2 Turnover in Arabidopsis Root Epidermal Cells Explored by the  
1379 Photoconvertible Protein Dendra2. *PLOS ONE* **8**, e61403 (2013).
- 1380 70. Brunoud, G. *et al.* A novel sensor to map auxin response and distribution at high spatio-temporal  
1381 resolution. *Nature* **482**, 103–106 (2012).
- 1382 71. Salanenko, Y. *et al.* Gibberellin DELLA signaling targets the retromer complex to redirect protein  
1383 trafficking to the plasma membrane. *Proc. Natl. Acad. Sci. U. S. A.* **115**, 3716–3721 (2018).
- 1384 72. Ulmasov, T., Murfett, J., Hagen, G. & Guilfoyle, T. J. Aux/IAA proteins repress expression of  
1385 reporter genes containing natural and highly active synthetic auxin response elements. *Plant*  
1386 *Cell* **9**, 1963–1971 (1997).
- 1387 73. Marin, E. *et al.* miR390, Arabidopsis TAS3 tasiRNAs, and Their AUXIN RESPONSE FACTOR Targets  
1388 Define an Autoregulatory Network Quantitatively Regulating Lateral Root Growth. *Plant Cell* **22**,  
1389 1104–1117 (2010).
- 1390 74. Colón-Carmona, A., You, R., Haimovitch-Gal, T. & Doerner, P. Technical advance: spatio-  
1391 temporal analysis of mitotic activity with a labile cyclin-GUS fusion protein. *Plant J. Cell Mol. Biol.*  
1392 **20**, 503–508 (1999).
- 1393 75. Glanc, M., Fendrych, M. & Friml, J. Mechanistic framework for cell-intrinsic re-establishment of  
1394 PIN2 polarity after cell division. *Nat. Plants* **4**, 1082–1088 (2018).

- 1395 76. Pasternak, T. *et al.* Protocol: an improved and universal procedure for whole-mount  
1396 immunolocalization in plants. *Plant Methods* **11**, 50 (2015).
- 1397 77. Johnson, A. & Vert, G. Single Event Resolution of Plant Plasma Membrane Protein Endocytosis  
1398 by TIRF Microscopy. *Front. Plant Sci.* **8**, 612 (2017).
- 1399 78. Hille, S., Akhmanova, M., Glanc, M., Johnson, A. & Friml, J. Relative Contribution of PIN-  
1400 Containing Secretory Vesicles and Plasma Membrane PINs to the Directed Auxin Transport:  
1401 Theoretical Estimation. *Int. J. Mol. Sci.* **19**, (2018).
- 1402 79. Schindelin, J. *et al.* Fiji: an open-source platform for biological-image analysis. *Nat. Methods* **9**,  
1403 676–682 (2012).
- 1404 80. Tinevez, J.-Y. *et al.* TrackMate: An open and extensible platform for single-particle tracking.  
1405 *Methods* **115**, 80–90 (2017).
- 1406 81. Lewis, D. R. & Muday, G. K. Measurement of auxin transport in *Arabidopsis thaliana*. *Nat. Protoc.*  
1407 **4**, 437–451 (2009).
- 1408 82. Arvidsson, S., Kwasniewski, M., Riaño-Pachón, D. M. & Mueller-Roeber, B. QuantPrime – a  
1409 flexible tool for reliable high-throughput primer design for quantitative PCR. *BMC Bioinformatics*  
1410 **9**, 465 (2008).
- 1411 83. Kuhn, M. *et al.* *caret: Classification and Regression Training*. (2020).
- 1412 84. Delignette-Muller, M. L. & Dutang, C. fitdistrplus: An R Package for Fitting Distributions. *J. Stat.*  
1413 *Softw.* **64**, 1–34 (2015).
- 1414 85. Rosario-Martinez, H. D., Fox, J. & R Core Team. *phia: Post-Hoc Interaction Analysis*. (2015).
- 1415 86. Lenth, R., Singmann, H., Love, J., Buerkner, P. & Herve, M. *emmeans: Estimated Marginal*  
1416 *Means, aka Least-Squares Means*. (2020).
- 1417 87. Hothorn, T. & Zeileis, A. partykit: A Modular Toolkit for Recursive Partytioning in R. *J. Mach.*  
1418 *Learn. Res.* **16**, 3905–3909 (2015).

- 1419 88. Karwowski, R. & Prusinkiewicz, P. The L-system-based plant-modeling environment L-studio  
1420 4.0 The L-system-based plant-modeling environment L-studio 4.0. in *Proceedings of the 4th*  
1421 *International Workshop on Functional-Structural Plant Models*, (2004).
- 1422 89. Stepanova, A. N. *et al.* TAA1-Mediated Auxin Biosynthesis Is Essential for Hormone Crosstalk and  
1423 Plant Development. *Cell* (2008) doi:10.1016/j.cell.2008.01.047.
- 1424 90. Xuan, W. *et al.* Cyclic programmed cell death stimulates hormone signaling and root  
1425 development in *Arabidopsis*. *Science* (2016) doi:10.1126/science.aad2776.
- 1426 91. Kleine-Vehn, J. *et al.* Differential degradation of PIN2 auxin efflux carrier by retromer-dependent  
1427 vacuolar targeting. *Proc. Natl. Acad. Sci. U. S. A.* (2008) doi:10.1073/pnas.0808073105.
- 1428 92. Mironova, V. V. *et al.* A plausible mechanism for auxin patterning along the developing root.  
1429 *BMC Syst. Biol.* (2010) doi:10.1186/1752-0509-4-98.
- 1430 93. R Development Core Team, R. *R: A Language and Environment for Statistical Computing*. R  
1431 *Foundation for Statistical Computing* (2011). doi:10.1007/978-3-540-74686-7.
- 1432 94. Ginestet, C. ggplot2: Elegant Graphics for Data Analysis. *J. R. Stat. Soc. Ser. A Stat. Soc.* (2011)  
1433 doi:10.1111/j.1467-985x.2010.00676\_9.x.
- 1434 95. Carpenter, B. *et al.* Stan: A probabilistic programming language. *J. Stat. Softw.* (2017)  
1435 doi:10.18637/jss.v076.i01.
- 1436 96. Bürkner, P. C. brms: An R package for Bayesian multilevel models using Stan. *J. Stat. Softw.*  
1437 (2017) doi:10.18637/jss.v080.i01.
- 1438 97. Vehtari, A., Gelman, A. & Gabry, J. Practical Bayesian model evaluation using leave-one-out  
1439 cross-validation and WAIC. *Stat. Comput.* (2017) doi:10.1007/s11222-016-9696-4.
- 1440 98. Sauer, M. *et al.* Canalization of auxin flow by Aux/IAA-ARF-dependent feedback regulation of PIN  
1441 polarity. *Genes Dev.* (2006) doi:10.1101/gad.390806.
- 1442 99. Wabnik, K. *et al.* Emergence of tissue polarization from synergy of intracellular and extracellular  
1443 auxin signaling. *Mol. Syst. Biol.* (2010) doi:10.1038/msb.2010.103.

- 1444 100. Yang, X., Dong, G., Palaniappan, K., Mi, G. & Baskin, T. I. Temperature-compensated cell  
1445 production rate and elongation zone length in the root of *Arabidopsis thaliana*. *Plant Cell*  
1446 *Environ.* (2017) doi:10.1111/pce.12855.  
1447